Theranostic Nanotoolbox for Medicated Pro-Regenerative Corneal Implants: Emerging Approaches in Ocular Tissue Engineering and Nanomedicine

Dr. Alejandro Rivera[1]*, Dr. Sofia Morales[1]
[1]National Autonomous University of Mexico Faculty of Medicine, Department of Ophthalmology and Biomedical Nanotechnology, Mexico City, Mexico

Keywords: Pre-medicated Cornea implant, Pro-regeneration, Theranostics, Herpes simplex virus type 1 (HSV-1), Magnetic resonance imaging (MRI)

Abstract

Cornea diseases are a leading cause of blindness and the disease burden is exacerbated by the increasing shortage around the world for cadaveric donor corneas. Despite the advances in the field of regenerative medicine, successful transplantation of laboratory made artificial corneas has not been fully realised in clinical practice. The causes of failure of such artificial corneal implants are multifactorial and include latent infections from viruses and other microbes, enzyme over-expression, implant degradation, extrusion or delayed epithelial regeneration. Therefore, there is an urgent unmet need for developing customized corneal implants to suit the host environment, counter the effects of inflammation or infection and that are able to track early signs of implant failure *in situ*. This present work reports a nano toolbox comprising tools for infection-protection, promotion of regeneration and non-invasive monitoring of *in situ* corneal environment. These nanosystems can be incorporated within pro-regenerative biosynthetic implants, transforming them into theranostic devices which are able to respond to biological changes following implantation.

1. Introduction

Transplantation of solid organs suffers from a dire shortage of donated tissues and organs, and issues of post-operative infection and immune rejection leading to graft failure. In corneal transplantation, the most common transplantation procedure, there is a shortfall of corneas that leaves an estimated 69 out of 70 patients with treatment delay and a waiting list of 12.7 million patient worldwide.[1] This does not include patients in remote areas, or those that may not be

prioritized for grafting due to high risk of rejection. Once a patient rejects a donor graft, the chances of the next graft being rejected are much higher, so the probability of each successive graft failing increases resulting in patients moving closer towards irreversible blindness.[2] Cornea transplantation is the only widely accepted treatment for restoring eyesight. However, corneas with severe pathologies, e.g. those causing inflammation or keratitis and severe vascularisation, are at high risk for rejecting conventional human donor transplantation.[3] The most common infectious cause for blindness worldwide is Herpes Simplex Keratitis (HSK), which is caused by the herpes simplex virus type 1 (HSV-1). In the USA alone, almost 500,000 cases of corneal HSV infection were reported with new and recurrent cases each year.[4,5] Approximately 20% of HSV-infected patients will develop HSK where the resulting scarring compromises vision sufficiently to require transplantation to restore eyesight. Patients with HSK are often prescribed lifelong prophylactic drugs to prevent reactivation, as reactivation can lead to graft rejection and failure. Systemic prophylactic drugs when required are often at higher doses to counter the pharmacokinetics of poor absorption through corneal layers and sub therapeutic levels reached within the eye.[6–8] Further, long term prophylaxis is sometimes associated with systemic side effects and cases of ACV-resistance have also been reported.

Artificial corneas in the form of prostheses known as keratoprostheses (or KPros) were developed for managing high-risk corneas.[9] One of the most successful KPros is the Boston KPro, comprising a synthetic poly methyl methacrylate (PMMA) optic and front plate. Together with a PMMA/titanium back plate,[10] the front and back plates are used to sandwich a skirt comprising a donor corneal graft. However, even in the Boston KPro, lifelong antibiotics are necessary to prevent infection due to incomplete bio integration of the device[11] and the device exposes the patients to a very high risk (60-76%) of glaucoma leading to non-reversible blindness. KPros are therefore only used in the case of end-stage disease[12] and a shunt is often co-implanted to manage glaucoma.[13] These implants are not medicated nor do they use materials that are aligned to human corneal collagen. Interestingly, there has been proposed co-

implantation of an intraocular pressure sensor embedded to detect glaucoma (ClinicalTrials.org identifier: NCT 03421548) but the trial was withdrawn.

Members of our team recently reported the successful 24 month grafting of cell-free, recombinant human collagen type III-methacryloyloxyethyl phosphorylcholinephospholipid (RHCIII-MPC) implants into keratitis patients[14]. One patient had HSK and the other had fungal keratitis. Both showed marked vision improvement at an average of 24 months post-grafting. Although the HSK patient was doing well at the 2-year check-up, HSV-1 infections can recur at any time due to prolonged viral latency in the trigeminal nerves that supply the cornea.[15] The surgical procedure and post-operative steroids have additionally been implicated in viral reactivation.[16] A complete theranostic implant system with *in situ* monitoring and detection function for viral reactivation and the ability to release drugs to block viral activity is therefore merited.

Our team previously used layer-by-layer nano-coating technology to engineer a contact lens that could detect elevated levels of interleukin-1, one of the earliest cytokines that initiate the inflammatory cascade in HSK.[17] The diagnostic component consisted of an antibody-chromophore colorimetric change in the presence of increased interleukin-1. However, the therapeutic aspect of this theranostic implant system was not well-developed. Therefore, we focus here on developing a complete integrative theranostic system with therapeutics and diagnostic ability. We examined the potential of a therapeutic, pro-regeneration corneal implant that incorporated acyclovir, a widely-used antiviral drug with gold nanoparticles (GNPs) to design a medicated device capable of regulated drug release following transplantation. We have developed and examined the possibility of tracking the drug profile within the implants using minimally invasive magnetic resonance imaging (MRI). We have simultaneously developed another nano tool by replacing the gold particles, which might not be readily traced under relatively dry eye conditions, with iron nanoparticles (FeNP) that have been widely used

for MRI tracing. We have developed a Nano toolbox that incorporates theranostic approach to combat major corneal issues by offering tools that are cornea compatible, release the appropriate drugs, promote the growth of epithelial cells and monitor the regeneration process non-invasively, to provide patients with personalised solutions. We show that these tools are easily incorporated into pro-regeneration corneal constructs, converting these customised artificial corneas into therapeutic implants (Tx). These Tx together with previously described diagnostic contact lenses constitute a theranostic system that can be further developed for a personalized clinical application.

2. Result and Discussion

2.1 Design, synthesis and characterization of the theranostic gold nanosystems

A range of gold nanoparticles (GNPs) were synthesized and one with 20nm hydrodynamic diameter and surface plasmon absorbance maximum at 520nm **(Figure 1A)** and surface zeta potential of -54mV were optimized[18] for our theranostic purpose for ACV conjugation and function. We optimized a non-covalent ionic coupling approach with the zwitterionic forms of ACV (with both the weak acid and basic moieties with pKa= 9.3 for ionization of the guanine OH, and pKb=2.3 for protonation of guanine nitrogen). The Hyperquad Simulation and Speciation (HySS) was used to analyse zwitterion features of ACV to obtain the optimal conditions with the required flexibility for conjugation **(Figure 1B)**.[19,20] Synthesized GNPs surface was capped with polybasic citrate **(Figure S1)**, which yields hydrogen at pH 6.4 and pH 4.7.

Therefore, above this pH, the GNP surface becomes negative, enabling ionic interactions with zwitterionic ACV.[21] A pH range from 6.4 to 9 was identified as the zwitterion zone (cyan; **Figure 1B**) that facilitated interaction with the activated GNPs surface for ACV loading. Upon conjugation with ACV, the size distribution of GNPs showed shift from 20 nm to ~81nm in hydrodynamic diameter, with an absorbance maximum at 528nm and zeta potential of -16.6mV.

Direct monitoring and conjugation of GNPs with the ACV was studied *in vitro* using a flocculation test[22] by increasing strength in presence of salt, NaCl (**Figure 1C**).

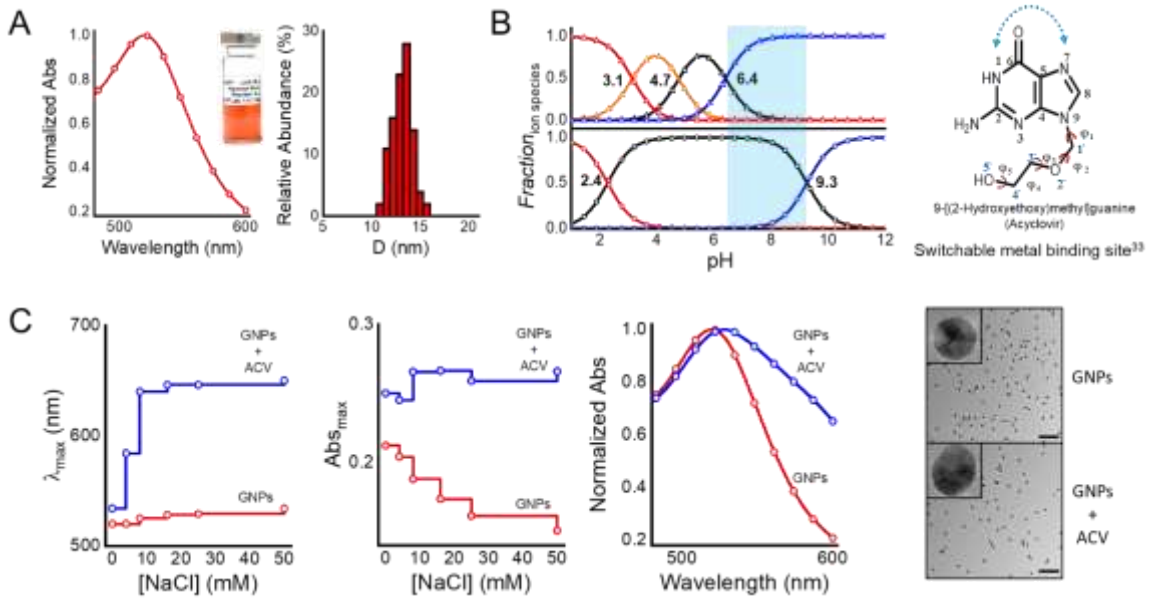

Figure 1. **Development of GNP nanosystem.** A, Left: Absorption spectrum for citrate capped GNPs used in this study. Right: Hydrodynamic diameter (Size) histogram for colloidal GNP solution used (inset). B, Left: Hyperquad simulation and speciation (HySS) of citrate and anti-viral drug acyclovir with indicated optimised zone for drug loading with loosely bound semi ionic Lewis bonds.[23] Right: The structural flexibility of acyclovir in facilitating conjugation. C, Functionalisation of acyclovir on the activated and optimized gold nano-surface by flocculation test (first two plots), shift in surface Plasmon absorption maxima λmax(third plot), and TEM images of both as synthesised and acyclovir-functionalised GNPs (scar bar = 100nm).

The result showed disruption of the ionic stability[23] between GNPs and ACV leading to the formation of large particle aggregates as represented by higher red shift in the λ_{max} for the conjugated species as opposed to the unconjugated GNPs (see *Supplementary section 3 for more molecular signature with FTIR*). A high concentration of NaCl perturbs the electrical double layer of the GNPs and induces a shift in the equilibrium between electrostatic repulsion and attraction of the particles.[22]

2.2 Composite collagen Tx.

Collagen implants comprising 10% (wt/wt) were fabricated as previously described.[24] A detailed description for the fabrication of therapeutic implants (Tx) with ACV-conjugated

GNPs (ACV-GNPs) is illustrated in **Figure S2**. The Tx constructs were optically transparent **(Figure 2A & S2)**. Cryo-scanning electron microscopy (cryo-SEM) imaging showed that the surfaces and cross sections of both Tx and unmodified biosynthetic cornea implants (Bx) shared similar surface features of interconnected lamellae **(Figure 2B, C)**. Detailed morphological analysis of the samples was conducted to compare the structural integrity of the Tx and Bx **(Figure 2D-F)**. The inner structural morphology remained conserved in Tx and there were no critical feature differences caused by the incorporation of the ACV-GNPs. Cryo-SEM through a cross-section of a Tx shows similar to Bx lamellate morphology. To assess biocompatibility, a degradation study was conducted to measure the relative resilience of Tx to collagenase degradation, compared to Bx without GNPs. Incorporation of GNPs did not decrease the stability of the hydrogel against Collagenase. Moreover, ~20% of the residual mass of the Tx hydrogel remained at 4 hours of the study when control hydrogel completely dissolved. However, Tx hydrogel also dissolve entirely at 5 hours **(Figure 2G)**. This can be due to the absorption of polymer chain onto the nanoparticle surface, which essentially increase the crosslinking density of the hydrogel.[25]

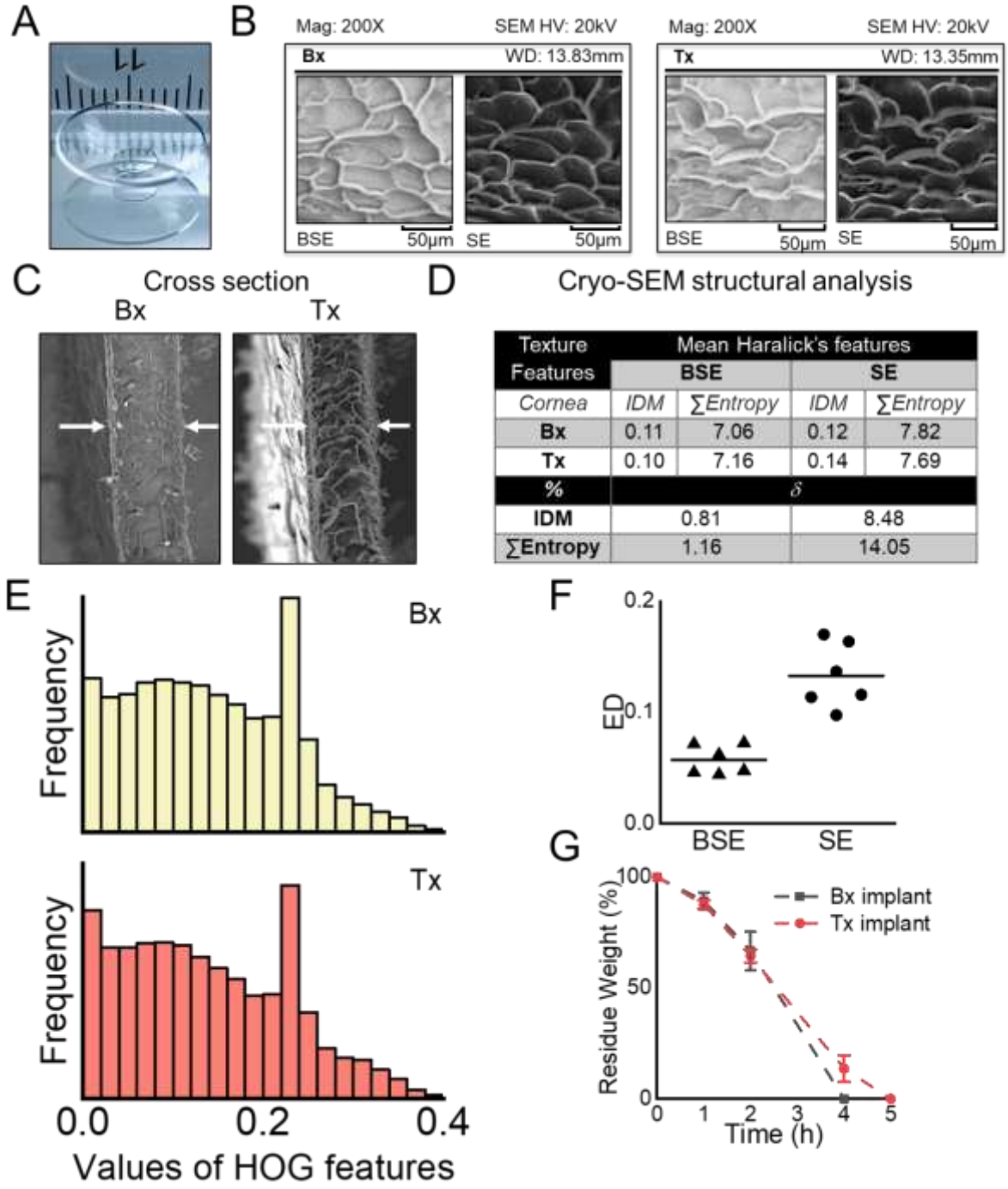

Texture Features	Mean Haralick's features			
	BSE		SE	
Cornea	*IDM*	*∑Entropy*	*IDM*	*∑Entropy*
Bx	0.11	7.06	0.12	7.82
Tx	0.10	7.16	0.14	7.69
%	δ			
IDM	0.81		8.48	
∑Entropy	1.16		14.05	

Figure 2. Tx implants. **A,** Physical form of the fabricated corneal implants. **B,** Cryo-Electron Microscopic (EM) features of unmodified control biosynthetic cornea (Bx) and Tx and their **C,** 100X cross-sections at 20KV. Backscattered-electron (BSE) images are for comparing compositions, information on topography and crystallinity, whereas secondary electron (SE) imaging are assessment for the topography of the cornea surface. (**D-F**) Morphological feature based on HOG and Haralick's texture to maintain the structural integrity in Tx. Inverse different moment (IDM) is the measure of local homogeneity and sum entropy reflects the measure of non-uniformity in the image during comparison of Bx and Tx electron microscopic features. **E,** Values of HOG features. **F,** Values of Euclidean distance (ED), in each distribution, the central mark is the median. **G,** In vitro biological stability test with collagenase.

A detailed histogram of oriented gradients (HOG) analysis together with study and illustration of Haralick's texture feature analysis show similar local homogeneity and non-uniformity in both Tx and Bx[26,27] (*detailed in supplementary section 2*). The summary table shows mostly identical physical features. Therefore, the integration of ACV-GNPs into collagen implants did not result in any significant structural perturbations in the overall nanoscale structure of the collagen lamellae.

2.3 Physical properties and biocompatibility of Tx implants

Rheological examination of implants showed that the storage modulus of the Tx was higher than those of control Bx, indicating stronger elastic response after incorporation of ACV-GNPs **(Figure S8A)**. The loss modulus (G″) represents the energy dissipated during shear, which indicates the ability of a material to disperse mechanical energy through internal molecular motions, and represents the viscous response of a material (**Figure S9**). The G″ of the Tx was higher than that of the Bx. This can again be explained by increase in crosslinking density due to the incorporation of GNPs.[25] When G′ > G″ (*tan* δ < 1), the hydrogel behaves more like an elastic solid, which was true for both implants (*Supplementary section 4*). Transmittance of white light was comparable between the two sets of formulations **(Figure S8B)**. Although, the transmittance was slightly higher in the Tx cornea than in the Bx, the increment is almost negligible. This also further confirms that integration of the nanosystem into the collagen implants did not result in transmission changes. Backscatter values for both Tx and control implants were also similar **(Figure S8C)**.

The thermal stability of Tx was examined and confirmed by differential scanning calorimetry (DSC). The thermal transition for the Bx was statistically significantly different ($p \leq 0.05$) than that of the Tx (**Figure S8C**). GFP-expressing human corneal epithelial cells (GFP-HCECs) seeded onto 3D composite Tx corneas proliferated at a higher rate over the five-day observation period than on Bx **(Figure S8D-E)**. The incorporation of GNPs or ACV-GNPs had no

observable cytotoxic effects and instead resulted in promoted proliferation (by more than 50% at 48h) when compared with Bx **(Figure S8D-E)**. Using different hydrodynamic sizes of GNPs, we also showed that GNPs can promote proliferation of HCECs (*supplementary section 5*) to different extents and this offers flexibility in selecting the GNPs[28,29] for custom-tuned Tx implants.

2.4 Antiviral activity of Tx implants

The antiviral activities of the Bx, Bx+ACV, and Tx were assessed using a viral focus forming assay (FFA). Viral proteins expressed by infected cells were detected using fluorescently-labelled antibodies, providing a more sensitive assay than the traditional plaque assay. Labelled infection foci are shown in **Figure 3**.

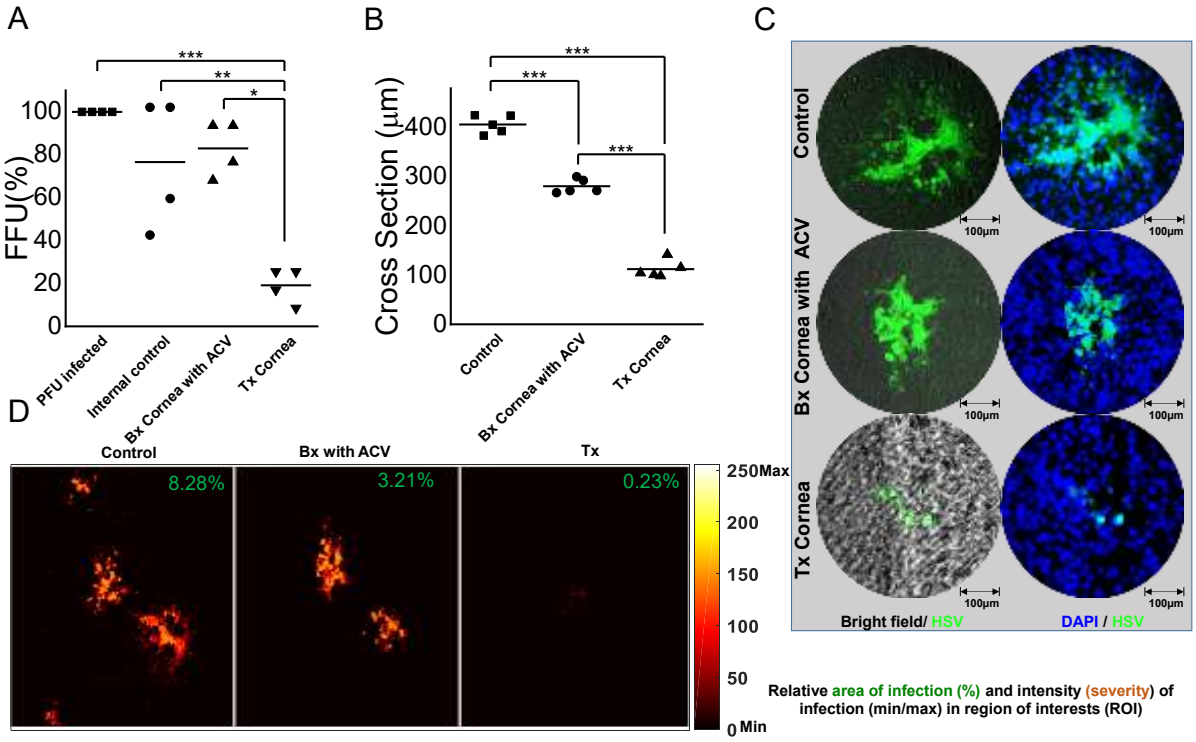

Figure 3. ***In vitro*** **Anti-HSV activity of Tx**. **A,** Comparative HSV infection measured using Focus forming assay (FFA) and expressed as % FFU (Focus Forming Unit) for direct determination of antiviral activity on the infected Tx. **B,** Relative infection cross section diameter (µm). **C,** Immune-stained individual virus infected focus using anti-HSV specific antibodies**. D,** Severity of the infection represented at Region of Interest (ROI) scaled image after HSV focus formation.

Here, an HSV 1/2 polyclonal antibody conjugated to FITC was used to stain HSV-1 transient exposure-infected confluent cells growing on the implant surface. Figure 3A shows the % focus forming units (FFU) present within cells cultured on collagen hydrogels (Bx, Bx+ACV, and Tx).

A marked reduction in the number of infected foci on Tx was observed compared with Bx+ACV ($p \leq 0.001$). In addition, a significant reduction in the size of infected cell foci on Tx compared with Bx ($p \leq 0.0001$). The FFA was specifically useful for quantifying the infection on a layer of human epithelial cells growing on three-dimensional, 500-µm thick corneal implants **(Figure 3C)**. Furthermore, a comparative quantification performed in a region of interest (ROI) **(Figure 3D)** by mapping the minimum and maximum intensity of the infection showed that on Tx, not only the number and size of infection foci, but also the relative intensity of fluorescence of the infected foci were greatly reduced compared with the controls.

2.5 Real time MRI monitoring of drug release from Tx implants

Non-invasive MRI assessments of the Tx microenvironment and tracking of the drug molecules in the transplanted implant would be a dramatic step toward corneal tissue regeneration procedure. Such microenvironment and the associated role player interactions with the other eye compartments determine the regenerative fate of transplanted cornea and are important in monitoring individual disease prognosis. However, there are few techniques that can assess these properties non-invasively, globally, in real time, and quantitatively. The Tx developed in this work provide the potential solution for such unmet needs. The Bx, Tx-ACV+ (fully loaded with ACV), and Tx-ACV- (no ACV, mimicking the releasing end stage) were scanned with MRI in transverse relaxivity (R2) mapping, proton density (PD)-weighted, and transverse relaxation (T2)-weighed modes. (**Figure 4A**). The incorporation of GNPs and ACV into the Tx had strong impacts on the R2 of the water molecules within the implant, providing desirable contrast under MRI. The difference in MRI contrast between Tx-ACV+ and Tx-ACV- can be

utilized to surveil the drug release profile by changing the MRI contrast R2. The drug releasing and retaining process was successfully monitored for 60 days (**Figure 4B**) including different initial drug dose (**Figure 4C**). While GNPs based Tx provided sufficient contrast by both transverse relaxation (T2) and the water content sensitive proton density (PD)[30] (**Figure 4A**), they are not ideal for precise monitoring associated water environment. The mapping of the extent of drug release is only possible with the enhanced contrast ability of the implants.

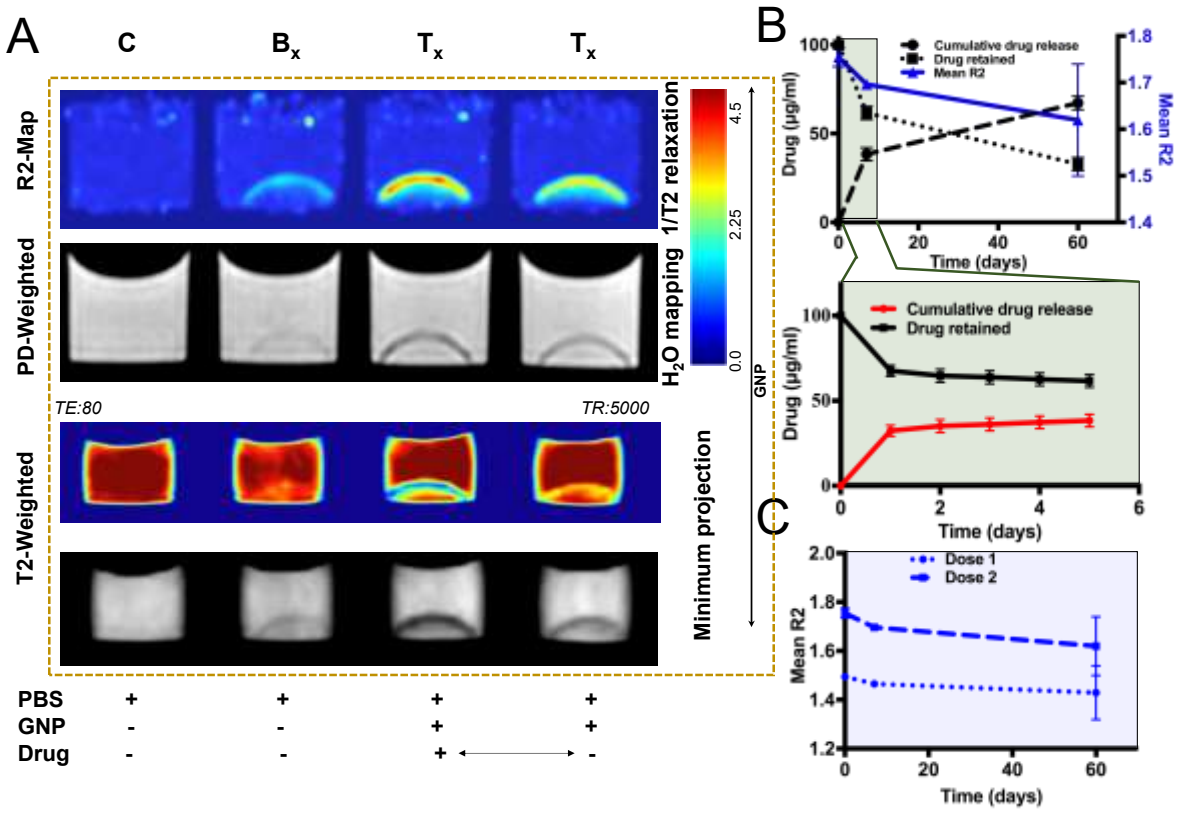

Figure 4. Theranostic corneal implant with realtime monitoring of drug retained non-invasively. **A**, MRI contrast using GNPs based nanosystems for transverse relaxation rate (R2 Map) and proton density weighted (PD-weighted) water mapping. Minimum projection of the transversal relaxation time T2-weighted MRI images in presence and absence of the loaded drugs (bottom panel). **B,** Extended cumulative release and retention profile of the antiviral drug (ACV) for two months **C,** Relative magnetic resonance imaging MRI contrast R2 (follow-up of the effective transverse relaxation rate) with two different doses of loaded drug in Tx.

To achieve even stronger contrast and to overcome the issues of mapping within the human cornea, a FeNP-based nanosystem for ACV delivery was developed to allow the use of multimodal MRI to track the corneal water environment and to correlate the amount of drugs present. **Figure 5A**, and the associated *Supplementary section 6*, shows the steps in the

incorporation of ACV-loaded FeNPs (ACV-FeNP) into these Tx and the biocompatibility of FeNPs with human corneal epithelial cells.

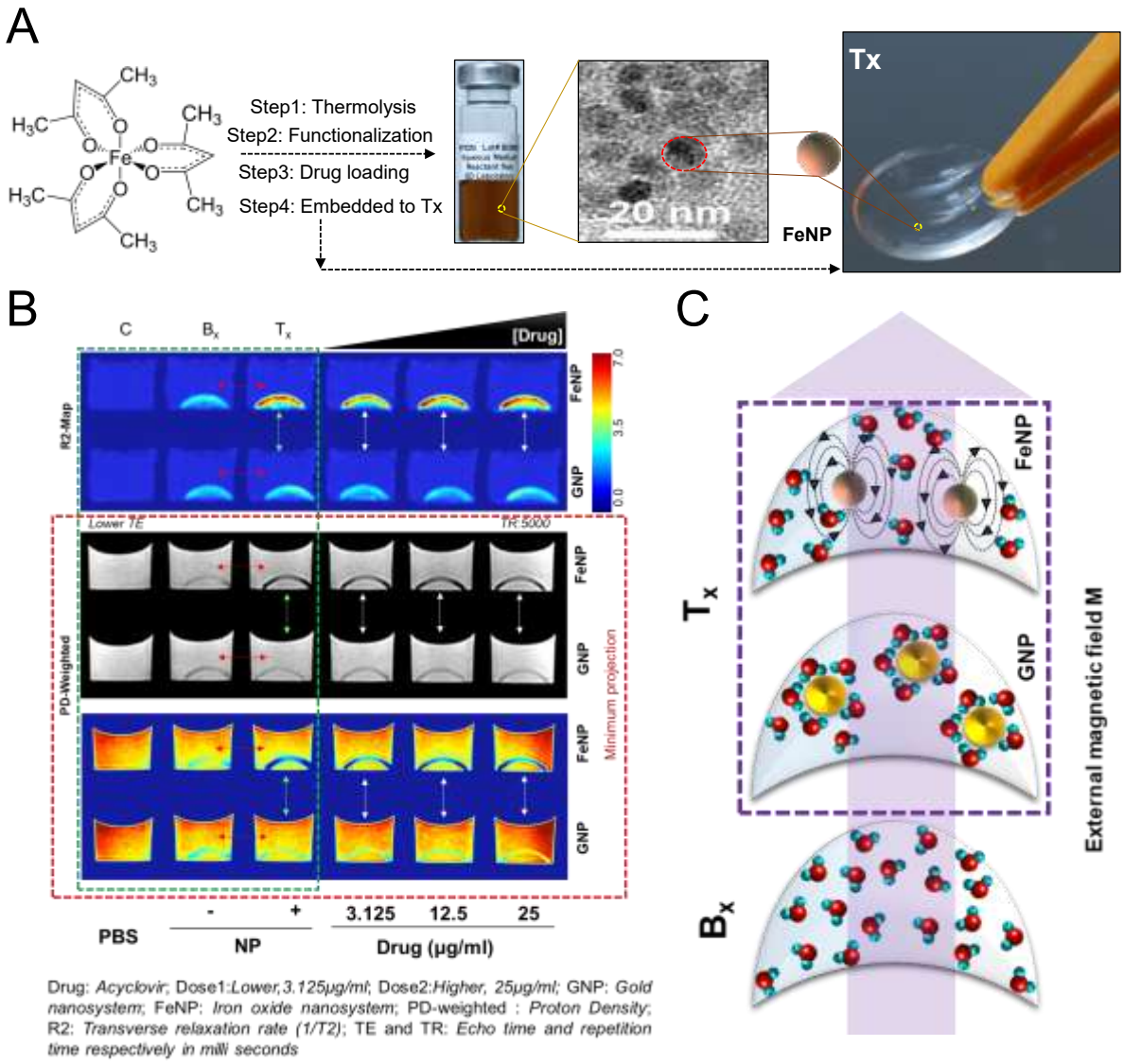

Figure 5. Tx implant for non-invasive monitoring. A, Schematic representation of the MRI-enabled iron based nanosystem developed for Tx. **B,** Quantitative and comparative MRI mapping of superparamagnetic iron oxide based nanosystem for development of enhanced MRI contrast Tx. Comparative R2 contrast in presence and absence of nanosystem indicated by red arrow (green box) and comparative MRI contrast on the extent of drugs present within the Tx indicated with white arrow. Local water environment can be observed with minimum projection in both GNPs and FeNPs based Tx for proton density weighted (PD-weighted) images and can be helpful indicator for infection, inflammation, integration and regeneration process of the Tx. **C,** Schematic illustration of the contrast effect influenced by the magnetic relaxation process of the protons in water molecules[30] of the nanosystems associated with Tx in the presence of external magnetic field during MRI.

The resulting FeNP based Tx when tracked using MRI, showed changing profiles that are related to the extent of drug present (**Figure 5B**). Detailed examination of the changing profiles

by T2 and PD weighted images showed that the changes in MRI contrast could be quantitatively correlated to the associated water environment and the amount of intra-corneal drug molecules present in a concentration dependent manner (as demonstrated in **Figure 5B**).

Figure 5C is a schematic that illustrates the possible interactions of nanosystems for ordering of water molecules that may account for mapping observation.

The MRI investigation of the Tx gives information about the morphological changes, ACV release extent, and hydrophobic microenvironment of the corneal implant at the same time. The morphological integrity of the corneal graft needs to be retained for a reasonably long enough time for regeneration to take place. Constant monitoring through non-invasive and non-ionising radiation of MRI for possible degradation and defects of the implants can greatly facilitate postoperative recovery. The extent of drug release from the implant also needs to be checked periodically after the implantation for fighting off possible infection. The corneal hydration level also needs to be maintained at a stable level for corneal regeneration. Abnormal levels of corneal hydration have been associated with corneal disorders such as corneal edema.[31] The hydration of the corneal implant can be inferred from both the morphological change (swelling) as well as the contrast change. The Tx therefore affords a comprehensive solution for corneal implant which allows all-around postoperative recovery and regeneration monitoring.

2.6 Discussion

A simple theranostics toolbox has been developed for pro-regenerative corneal implants with functionalities suitable for an effective alternative to human donor cornea. A theranostic approach is needed for patients at high risk of rejecting implants in a model system such as with HSK, where viral reactivation is very well documented. The ideal theranostic approach should consider patient safety and selectivity for the site of action, possess the ability to diagnose disease conditions and provide efficient delivery of therapeutics agents. The diagnostic component required to track viral reactivation. An indirect example of such kind is detection of a cytokine that plays major role in activation of the inflammatory cascade associated with

disease recurrence.[17] Current results show that it is possible to integrate the therapeutic component of the implantation-cum-monitoring theranostic package into the implants. As such we have selected components that will allow for safe clearance from the body as they are or as degraded nontoxic products, or integration within the body.[31,32]

As a backbone of this work, we used the formulation of the biosynthetic cornea that has been shown to promote effective regeneration of corneal tissue and nerves in a mini-pig model.[24] ACV, a widely used antiviral agent was selected as this or a variant is likely to be the drug of choice in treatment of patients with HSK. Being hydrophobic and highly insoluble in aqueous solutions, ACV offers very limited opportunity to modify and retain its functional activity[33] to inhibit viral DNA polymerase enzyme to stop viral replication. ACV also has low permeability[34] that makes difficult to formulate prophylaxis.[35] Direct incorporation of ACV within collagen hydrogels resulted in burst release and rapid diffusion of drug out of the polymer matrix[36] GNPs were therefore used as a carriers for ACV, and the ACV-GNPs were then incorporated into the collagen-based implants. Our results showed that GNPs can be loaded with ACV within the zwitterionic range of the drug. The hydrodynamic diameter of the drug loaded particles increased from 20 to 81 nm. This was the case in our Tx where there were no changes to the optical transparency after loading of ACV-GNPs. In an earlier report ACV has been released from silica nanoparticles[37] embedded within hydrogel and anti-viral activity measured with the released media but never been tried to make the implant pre-medicated and infect the corneal cells on the implants with virus. In this study, we tethered ACV to GNPs for delivery. Once released, the ACV was fully potent and able to stop HSV-1 activity. Furthermore, the ACV had no adverse effects on cell proliferation at the doses used and in fact, proliferation rates were enhanced in the presence of GNPs. The proliferation rate of HCECs was higher, which could be a feature of a mechanically stiffer hydrogels or confirmation of reports that the presence of GNPs can promote cell growth.[28]

The regeneration of corneal tissues and nerves can be assessed in real-time by *in vivo* confocal microscopy in animal models[38] or patients.[39] However, this technique is limited by topographic repeatability in addition to lack of global representation[40] and is unable to track the amount of drug infused or released. MRI is commonly used in health care centres to obtain detailed images within the body without exposure to radiation with the help of gadolinium and iron-based contrast agents. Here, we showed that FeNPs could be incorporated into Tx to probe the extent of drugs release from the implants as monitored by MRI reflected the release of ACV. The capacity to track the local environment through proton density is particularly important during corneal pathogenesis.[41,42] Reactivation of the virus in the implanted eye in the clinical setting can range from few days to months and hence the retention of drugs is important to keep them pre-medicated for prolong period to combat against reactivation. More importantly, this approach can pay way in future therapeutics by releasing recombinant nerve growth factors to address vital issues such as in case of delayed epithelialization. It is also possible that the pattern of contrast in the MRI images will change as neo-tissue is regenerated within the implants, and as the implants are remodelled. The evaluation of Tx and control implants within implanted corneas in animal models, and the diagnostic contact lens previously developed will be an important next step in the integration of theranostic implant and monitoring system for future translation.

3. Conclusion

Cell-free, pro-regeneration collagen-based corneal implants incorporating nanosystems releasing ACV have the potential to prevent peri-operational reactivation of HSV-1 viruses in compromised corneas. Together with contact lenses that were previously developed to detect interleukin-1 as an inflammation marker, we demonstrate the feasibility of a two-part theranostic system for use in HSK corneas at high risk of rejection due to disease recurrence. While *in vivo* feasibility testing in animal models is merited, we have demonstrated the

feasibility of a theranostic system that could be used to deliver drugs and other bioactive molecules to the cornea and to allow precise monitoring through a combination of MRI and clinically available *in vivo* confocal microscopy. This “nano toolbox” with its precise monitoring capability will have an important role particularly in the pre-clinical safety and efficacy testing of new composite implants with therapeutic functions. Further development of the toolbox will allow fabrication of customised implants for patients.

4. Experimental Section

4.1 Synthesis of GNPs and conjugation with ACV

GNPs were synthesized using Turkevich and Frens method with required modifications.[43] Briefly, an aqueous solution of $HAuCl_4$ (Sigma-Aldrich, St Louis, MO, USA; 250µM, 25mL) was heated at 90-95°C, close to boiling condition, while stirred continuously with a magnetic stirrer. Freshly prepared 100mM trisodium citrate dihydrate (Sigma-Aldrich, St Louis, MO, USA) solution was then added at once, in different amounts (final concentrations 1200, 600, 400, 200 and 100µM) depending on the desirable particle size (*Supplementary section 1*). The solution was heated up for additional 25 minutes, resulting in a change of solution colour from pale yellow to orange for smaller particles or purple for bigger ones. After obtaining a persistent colour the solution was allowed to cool down to room temperature. The purified stock solution of GNPs was obtained by precipitating and dispersing in ambient medium. For this, 20ml of GNPs solution was centrifuged at 7500 rpm and the supernatant was discarded. This is done to reduce the formation of additional citrate layers between the adsorbed citrate on the surface of the GNPs and the free citrate ions available in the solution and also to remove free Cl- and acetone decarboxylate formed during the course of the reaction process. The centrifuged GNPs were re-suspended in trisodium citrate/citrate buffer and the pH of the re-suspended GNPs colloidal solution was kept above 6.0 for further conjugation process. The purified colloidal suspension of GNPs was kept at 4ºC for further use.

Acycloguanosine (synonym of ACV; HPLC grade) was purchased from Sigma-Aldrich (St Louis, MO, USA). Stock solution of ACV was prepared in DMSO (10mg/ml) (Sigma-Aldrich, St Louis, MO, USA). From the purified/concentrated solution of GNPs, 23.78µg/ml of GNPs was used and to this 100µg/ml of ACV was added dropwise. The pH of the purified nanomaterials should be above 6.0, to allow for the conjugation of zwitterionic ampholyte ACV to easily bind to the surface of GNPs through ionic interaction between the negative citrate ions of the surface of the nanoparticles and the basic $–NH_2$ groups in ACV.

4.2 Synthesis of magnetic nanoparticles and conjugation with ACV

FeNPs were synthesized by thermal decomposition of Iron acetylacetonate (Sigma-Aldrich, St Louis, MO, USA). In brief, the dissolved iron acetylacetonate in benzyl ether (Sigma-Aldrich, St Louis, MO, USA) and oleylamine (Sigma-Aldrich, St Louis, MO, USA) mixture was heated at 110 ºC degree in nitrogen environment. This mixture was then reheated at 310°C for 2 more hours followed by cooling down to room temperature before it was mixed with 60ml ethanol. The suspension was centrifuged at 3000 rpm for 20 min and the supernatant was discarded and the precipitate was allowed to air-dry before resuspension in 20 ml hexane (Sigma-Aldrich, St Louis, MO, USA). The mixture was then been centrifuged at 25000g for one hour to remove larger particles and the supernatant was collected for functionalization.

Homo-dicarboxylic polyethylene glycol (PEG-2kd) (JenKem, USA), dimethyl formamide (Sigma-Aldrich, St Louis, MO, USA), chloroform (Sigma-Aldrich, St Louis, MO, USA), and N-ethyl-N-(3-dimethyl aminopropyl) carbodiimide hydrochloride (EDC) (Thermo Fisher Scientific, USA) were mixed in a reaction flask. The mixture was then stirred at room temperature for 30 minutes. Next dopamine (Sigma-Aldrich, St Louis, MO, USA) was added to the mixture and stirred at room temperature for 90 minutes followed bythe addition of oleylamine coated synthesized nanoparticles to the reaction vessel and overnight stirring at room temperature. Particles were allowed to settle down and washed with hexane, followed by

drying. The particles are suspended in water and were centrifuged 3000 rpm for 20 min to remove any aggregates formed. Then the particle suspension was spun at 2500-3000 rpm for 40 mins in nano-sep (Pall Pvt Ltd, MI, USA) (10 kd) to remove un-reacted PEG, and finally suspended in citrate buffer at around pH 7.5 to allow the binding of the zwitterionic ampholyte ACV to the surface of FeNPs through ionic interaction between the negative carboxyl ions of the surface of the nanoparticles and the basic $–NH_2$ groups in ACV.

4.3 Flocculation test

GNPs and GNPs-ACV were incubated with different concentrations of NaCl solutions (4, 8, 16, 25 and 50 mM) in a 1:1 volume ratio. All the samples were incubated at room temperature for 10 minutes and the hydrodynamic diameter, zeta potential and UV-visible absorbance were measured.[44]

4.4 Dynamic Light Scattering (DLS), Zeta Potential and UV-Visible absorption measurement

The hydrodynamic diameters (HD) and Zeta potential (ξ) measurements for both bio-conjugated and unconjugated nanomaterials under investigations were performed using a Zeta Sizer Nano ZS90 equipped with a red (633nm) laser (Malvern Instruments Ltd., England). All reported HDs are based on averaged intensity. For each sample, three measurements were conducted with a fixed 10 runs each. The same instrument was used to measure the ξ of the particles in the colloidal suspension by analysing the relative velocity of the particles with respect to the fluid. Again, for each sample three measurements were performed with a fixed 10 runs each. All the UV-Vis experiments were conducted using Thermo UV-Visible Spectrophotometer (Lambda 25, PerkinElmer, Akron, OH, USA).

4.5 Fourier Transformed Infrared Spectroscopy (FTIR)

Surface characteristic changes of GNPs after conjugation of ACV were determined by Attenuated Total Reflectance (ATR-FTIR). The measurements were performed using a PIKE MIRacle ATR accessory with a diamond prism in a vertex 70 Spectrometer (Bruker, Massachusetts, USA) with a DLaTGS detector. The whole system was continuously purged with nitrogen and the IR spectra were acquired at 4cm-1 resolution. A total of 64 scans were performed between 4400-600 cm^{-1}.

4.6 Fabrication of implants

Briefly, 0.5ml (~500mg) of 18% (wt/wt) porcine collagen solution type 1 (Nippon Meat Packers, Japan) was added in a syringe mixing system as previously described[24] and buffered with 150 µl of 0.625 M morpholinoethanesulfonic acid buffer (MES, EMD Chemicals, Gibbstown, NJ). Calculated amounts of N-Hydroxysuccinimide (NHS; Sigma-Aldrich, MO, USA) (5% (w/v) in MES) and N-(-3-Dimethylaminopropyl)-N'-ethylcarbodiimide hydrochloride (EDC; Sigma–Aldrich, MO, USA) (5% (w/v) in MES) solutions were added and the reactants were thoroughly mixed at 0°C (EDC: collagen–NH2 (mol:mol) = 0.7:1, EDC:NHS (mol:mol) = 1:0.5). The final mixed solution was immediately cast into cornea-shaped moulds (12 mm diameter, 500 µm thick) or between two glass plates with 500 µm spacers and kept at 100% humidity at room temperature for 24 hrs and then at 37°C for 1 hr. Hydrogels were then carefully remoulded and kept in 10 mM PBS at 4ºC. Two different types of collagen corneal implants were prepared (i) Biosynthetic cornea without any nanosystems (Bs) and (ii) nanosystem (GNPs, FeNPs) embedded theranostic cornea (Tx). The final concentrations of the different nanosystems and loading of ACV adjusted accordingly within the collagen matrix are mentioned in respective figures. In all cases, the additives were added to collagen mixing system before adding EDC and the volume was adjusted to keep the final concentration of collagen at 10% (wt/vol). In the control-without any nanosystems and ACV hydrogel, respective amount of buffer was added to keep the dilution factor the same as that of

experimental cornea. This formulation was used in all characterization and *in-vitro* studies unless stated otherwise.

4.7 Characterization of implants

White light transmission and backscattering of hydrogels were determined at RT on a custom-built instrument.[45] Differential scanning calorimetry (DSC) was performed using a Q2000 differential scanning calorimeter (TA instruments, New Castle, DE) as previously described[46] to measure the thermal transition and evaluate the degree of cross-linking in the hydrogels. Heating scans were recorded within the range of 8 to 80°C at a scan rate of 5°C min^{-1}. Samples weighing in the range of 4 to 7 mg were surface-dried and hermetically sealed in an aluminium pan to prevent water evaporation. A resulting heat flux versus temperature curve was then used to calculate the denaturing temperature (T_d). Denaturing temperature comes from the T_{max} of the endothermic peak. Mechanical properties of hydrogels were measured using a parallel plate rheometer (AR 2000 rheometer, TA instruments, Inc., UK). Hydrogels were trephined in cylindrical shape (500um thick, 8mm diameter) and storage modulus (G') and loss modulus (G'') measurements were recorded at a frequency range of 1-8Hz at 25°C using 8mm aluminium plate geometry. The gap was corrected starting from the sample height and compressing the sample to reach the sample to reach a normal force of 0.3N. The morphology of the biosynthetic hydrogel cornea constructs (with and without nanoparticles and anti-viral drug) was studied using scanning electron microscopy (SEM). Processing of the hydrogel prior to conducting SEM has been performed as described previously.[47] SEM micrographs were obtained at 20kV at various magnifications on a scanning electron microscope (Model S225ON, Hitachi, Japan). Comparisons were drawn against the control Bx (without drug and nanomaterials) and Tx cornea (containing the bio conjugated anti-viral drug and nanoparticles).

4.8 ACV release study

ACV-GNP containing hydrogels were transferred into a 50ml centrifuge tube containing 15ml 10mM PBS to keep the whole hydrogel immersed in the liquid. The tubes were then placed in a continuous mechanical shaker with 100rpm rotation at 37°C. The buffer in the tubes were collected at day 1, 2, 3, 4 and 5 and substituted with fresh buffer. The absorbance spectra of collected PBS buffers were recorded at 250nm using Thermo UV-Visible Spectrophotometer (Lambda 25, PerkinElmer, Akron, OH, USA) and the cumulative release of ACV from the hydrogel construct was evaluated using a standard ACV curve.

4.9 In vitro cell adhesion and proliferation assays

To examine the cell attachment and proliferation rate on different surfaces, green fluorescent protein (GFP) transfected, immortalised human corneal epithelial cells (HCECs)[48] were seeded (5000 cells/well) onto 6mm hydrogel discs in a 96-well plate. The GFP-HCECs were maintained in keratinocyte serum-free medium (KSFM; Life Technologies, Invitrogen, Paisley, UK), supplemented with 50 µg/ml bovine pituitary extract and 5 ng/ml epidermal growth factor, in a 37°C incubator with 5% CO_2. As controls, cells were also seeded on a regular tissue culture plate (TCP) and on a non-binding surface plate (data not shown). At 4, 24, 48, 72, 96 and 120 hrs, images of three different areas on each hydrogel disc were captured using a fluorescence microscope (AxioVert A1, Carl Zeiss, Gottingen, Germany) for quantitation.

4.10 Cell viability assay

Cell viability after incubation with the different GNPs and FeNPs concentrations were determined using the MTS assay, which is based on the reduction of MTS (3-(4,5-dimethylthiazol-2-yl)- 5- (3-carboxymethoxyphenyl)-2- (4-sulfophenyl)- 2H-tetrazolium) compound by living and metabolically active cells to generate a soluble coloured formazan derivative. HCECs were sub-cultured in 96-well plates containing 100µl of the culture medium. Twenty-eight thousand HCECs were seeded into each well. The cells were treated for 12, 24 and 48 hrs with GNPs and GNPs-ACV. After that, 20% v/v of MTS reagent in cell culture

medium was added and cultures were incubated further for 3 h at 37°C. Absorbance was measured at 490 nm and 650 nm as a reference using a spectrophotometric microplate reader (VERSA Max Microplate Reader, Molecular Device, Sunnyvale, CA, USA). Each sample was tested in triplicates and the average survival percentage was calculated with respect to the control (no GNPs/GNPs-ACV added). Before the addition of the MTS reagent, microscopic imaging (AxioVert A1, Carl Zeiss, Gottingen, Germany) was performed to assess the viability of the cells.

4.11 In-vitro fluorescent focal assay (FFA) for viral count

The antiviral property of the hydrogel containing GNPs with/without ACV was evaluated. Hydrogels were cut at 6mm diameter and placed in a 96-well plates. Forty thousand HCECs were cultured on these hydrogels until they were confluent. Cells were then infected for one hour at 37°C with the HSV-1, strain F (a gift from Earl Brown, University of Ottawa, Ontario, Canada) at a concentration of 6 plaque forming units (PFU) per each well to avoid overlap and distinctly observe individual focus. A negative control was used containing uninfected cells and a positive control containing cells infected with the virus and without GNPs. Each different treatment was tested in triplicate. The cells were washed in phosphate-buffered saline (PBS; ThermoFisher Scientific, Waltham, Massachusetts, USA) and 100µl of new medium were added to each well. The infected monolayer was incubated at 37°C in 5% CO_2 until the observation of plaques (approximately 24 hrs). The cells were then washed in cold PBS and fixed overnight in ice-cold absolute methanol. Next day the cells were washed twice with PBS in RT and incubated with HSV 1/2 polyclonal antibody FITC conjugate (ThermoFisher Scientific) at a dilution of 1:100 in PBS for 3hrs at RT and then washed twice in PBS. The cells were mounted in 1:1 glycerol-PBS and imaged using a fluorescence microscope (Leica DMi8, Leica, Wetzlar, Germany). Fluorescent focus units (FFU) located in each well were counted and virus titers were calculated and expressed as percentage (%) FFU with respect to control.

4.12 Tx implant stability study

Briefly, hydrated cross-linked hydrogels (8mm diameter) were placed in vials containing 5 U/ml collagenase (Type IA Collagenase from Clostridium histolyticum, 125 CDU/mg solid, Sigma-Aldrich, MO, USA) in 4 ml of 0.1M Tris-HCl (pH 7.4) buffer containing 5mM $CaCl_2$. The vials were incubated in an oven at 37°C. The gels were weighed at different time intervals after removal of surface water. The percent residual weight of the sample was measured based on initial mass.

4.13 Statistical analysis

Unpaired t-test was performed to compare each different intervention with the control. Values are represented as mean ± S.D. A p value<0.05 was considered statistically significant. All the tests were performed on MATLAB analysis software (MATLAB 2016B, Mathworks, USA).

Magnetic Resonance Imaging and Analysis: All MR-images were acquired with a 32-channel head coil in Philips Ingenia 3.0T scanner (Royal Philips, Amsterdam, Netherlands). Proton density weighted images were acquired using a multi-slice turbo spin-echo sequence, TR 6 sec, effective TE 8 ms, flip angle 90°, bandwidth 348 Hz, acquired in-plane resolution 0.6×0.6 mm^2, slice thickness 0.8 mm and a turbo factor of 15. T2-weighted images and R2-maps (1/T2) were generated on the scanner based on a multi-echo turbo spin-echo sequence with 20 echoes, first TE 10 ms, delta-TE 10 ms, TR 5 sec, flip angle 90°, bandwidth 177 Hz, acquired in-plane resolution 0.6×0.6 mm^2, slice thickness 1.3 mm and a turbo factor of 20. Minimum intensity images were generated using OsiriX (Pixmeo SARL, Geneva, Switzerland).

Supporting Information
Supporting Information is available from the Wiley Online Library or from the author.

Acknowledgements

We cordially thank Emilio Alarcon from University of Ottawa, Canada for helping with scanning electron miscopy experiment and May Griffith from Linkoping University, Sweden

for providing research materials and laboratory set up together with their valuable inputs during MS preparation. This work was supported by EU H2020 Marie Sklodowska-Curie Individual Fellowship (Grant no: 706694), MIIC Strategic Postdoc Grant and MIIC Seed Grant at Linkoping University (LiU), Sweden. We thank Magnus Borga for providing us the magnetic measurement facilities at CMIV, LiU and for his helpful inputs before designing the magnetic study. M. Azharuddin, M. M. Islam, and G. Papapavlou contributed equally to this work. J. Hinkula, M. S. Rajan, and N. K.H. Slater contributed equally to this work.

Received: ((will be filled in by the editorial staff))
Revised: ((will be filled in by the editorial staff))
Published online: ((will be filled in by the editorial staff))

References

[1] P. Gain, R. Jullienne, Z. He, M. Aldossary, S. Acquart, F. Cognasse, G. Thuret, *JAMA Ophthalmol.* **2016**, *134*, 167.

[2] A. Di Zazzo, A. Kheirkhah, T. B. Abud, S. Goyal, R. Dana, *Surv. Ophthalmol.* **2017**, *62*, 816.

[3] K. A. Williams, M. Lowe, C. Bartlett, T.-L. Kelly, D. J. Coster, *Transplantation* **2008**, *86*, 1720.

[4] M. Halberstadt, *Br. J. Ophthalmol.* **2002**, *86*, 646.

[5] M. L. Liesegang TJ, *Arch Ophthalmol* **1989**, *1*, 1982.

[6] E. Miserocchi, G. Modorati, L. Galli, P. Rama, *Am. J. Ophthalmol.* **2007**, *144*, 547.

[7] E. J. Ariza-Heredia, R. F. Chemaly, L. R. Shahani, Y. Jang, R. E. Champlin, V. E. Mulanovich, *Transpl. Int.* **2018**, *31*, 639.

[8] M. Van Velzen, D. A. M. C. Van De Vijver, F. B. Van Loenen, A. D. M. E. Osterhaus, L. Remeijer, G. M. G. M. Verjans, *J. Infect. Dis.* **2013**, *208*, 1359.

[9] V. S. Avadhanam, H. E. Smith, C. Liu, *Clin. Ophthalmol.* **2015**, *9*, 697.

[10] W. B. Lee, R. M. Shtein, S. C. Kaufman, S. X. Deng, M. I. Rosenblatt, F. Lum, *Ophthalmology* **2015**, *122*, 1504.

[11] M. Nouri, *Arch. Ophthalmol.* **2001**, *119*, 484.

[12] V. S. Avadhanam, C. S. C. Liu, *Br. J. Ophthalmol.* **2015**, *99*, 878.

[13] P. Nguyen, V. Chopra, *Curr. Opin. Ophthalmol.* **2014**, *25*, 134.

[14] M. M. Islam, O. Buznyk, J. C. Reddy, N. Pasyechnikova, E. I. Alarcon, S. Hayes, P. Lewis, P. Fagerholm, C. He, S. Iakymenko, W. Liu, K. M. Meek, V. S. Sangwan, M. Griffith, *npj Regen. Med.* **2018**, *3*, 2.

[15] S. K. H. S. K. Holland EJ, Schwartz GS, in *Cornea* (Ed.: M.M. and E. Holland), **2017**, pp. 909–941.

[16] P. Y. Robert, J. P. Adenis, F. Denis, S. Alain, S. Ranger-Rogez, *J. Med. Virol.* **2003**, *71*, 69.

[17] W. C. Mak, K. Y. Cheung, J. Orban, C. J. Lee, A. P. F. Turner, M. Griffith, *ACS Appl. Mater. Interfaces* **2015**, *7*, 25487.

[18] H. K. Patra, A. K. Dasgupta, S. Sarkar, I. Biswas, A. Chattopadhyay, *Cancer Nanotechnol.* **2011**, *2*, 37.

[19] M. Alvarez-Ros, M. Palafox, *Pharmaceuticals* **2014**, *7*, 695.

[20] L. Alderighi, P. Gans, A. Ienco, D. Peters, A. Sabatini, A. Vacca, *Coord. Chem. Rev.* **1999**, *184*, 311.

[21] S. Ghosh, D. Khatua, J. Dey, *Langmuir* **2011**, *27*, 5184.

[22] N. A. Byzova, I. V. Safenkova, E. S. Slutskaya, A. V. Zherdev, B. B. Dzantiev, *Bioconjug. Chem.* **2017**, *28*, 2737.

[23] H. Li, L. J. Rothberg, *J. Am. Chem. Soc.* **2004**, *126*, 10958.

[24] Y. Liu, L. Gan, D. J. Carlsson, P. Fagerholm, N. Lagali, M. A. Watsky, R. Munger, W. G. Hodge, D. Priest, M. Griffith, *Investig. Ophthalmol. Vis. Sci.* **2006**, *47*, 1869.

[25] S. Rose, A. Prevoteau, P. Elzière, D. Hourdet, A. Marcellan, L. Leibler, *Nature* **2014**, *505*, 382.

[26] R. M. Haralick, K. Shanmugam, I. Dinstein, *IEEE Trans. Syst. Man. Cybern.* **1973**, *SMC-3*, 610.

[27] N. Dalal, B. Triggs, in *2005 IEEE Comput. Soc. Conf. Comput. Vis. Pattern Recognit.*, IEEE, **n.d.**, pp. 886–893.

[28] H. K. Patra, A. K. Dasgupta, *Nanomedicine Nanotechnology, Biol. Med.* **2012**, *8*, 842.

[29] D. Liu, J. Zhang, C. Yi, M. Yang, *Chinese Sci. Bull.* **2010**, *55*, 1013.

[30] Y. Jun, J. Choi, J. Cheon, *Chem. Commun.* **2007**, 1203.

[31] F. Chen, E. B. Ehlerding, W. Cai, *J. Nucl. Med.* **2014**, *55*, 1919.

[32] A. Tiwari, H. K. Patra, J.-W. Choi, Eds. , *Advanced Theranostic Materials*, John Wiley & Sons, Inc., Hoboken, NJ, USA, **2015**.

[33] L. M. Beauchamp, B. L. Dolmatch, H. J. Schaeffer, P. Collins, D. J. Bauer, P. M. Keller, J. A. Fyfe, *J. Med. Chem.* **1985**, *28*, 982.

[34] L. Colla, E. De Clercq, R. Busson, H. Vanderhaeghe, *J. Med. Chem.* **1983**, *26*, 602.

[35] A. Mahmood, M. Ahmad, R. M. Sarfraz, M. U. Minhas, A. Yaqoob, *Acta Pol. Pharm. - Drug Res.* **2016**, *73*, 1311.

[36] T. T. Dang, A. V. Thai, J. Cohen, J. E. Slosberg, K. Siniakowicz, J. C. Doloff, M. Ma, J. Hollister-Lock, K. M. Tang, Z. Gu, H. Cheng, G. C. Weir, R. Langer, D. G. Anderson, *Biomaterials* **2013**, *34*, 5792.

[37] B. Bareiss, M. Ghorbani, F. Li, J. A. Blake, J. C. Scaiano, J. Zhang, C. Deng, K. Merrett, J. L. Harden, F. Diaz-Mitoma, M. Griffith, *Open Tissue Eng. Regen. Med. J.* **2010**, *3*, 10.

[38] J. V. Jester, N. Morishige, L. BenMohamed, D. J. Brown, N. Osorio, C. Hsiang, G. C. Perng, C. Jones, S. L. Wechsler, *Cornea* **2015**, *35*, 81.

[39] P. Fagerholm, N. S. Lagali, J. A. Ong, K. Merrett, W. B. Jackson, J. W. Polarek, E. J. Suuronen, Y. Liu, I. Brunette, M. Griffith, *Biomaterials* **2014**, *35*, 2420.

[40] T. Hillenaar, In Vivo Confocal Microscopy Expanding Horizons in Corneal Imaging, Erasmus University Rotterdam, **2012**.

[41] A. W. J. M. Glaudemans, A. M. Quintero, A. Signore, *Eur. J. Nucl. Med. Mol. Imaging* **2012**, *39*, 745.

[42] A. Neuwelt, N. Sidhu, C.-A. A. Hu, G. Mlady, S. C. Eberhardt, L. O. Sillerud, *Am. J.*

Roentgenol. **2015**, *204*, W302.

[43] H. K. Patra, D. GuhaSarkar, A. K. Dasgupta, *Anal. Chim. Acta* **2009**, *649*, 128.

[44] H. Jans, L. Austin, H. Jans, X. Liu, L. Austin, G. Maes, Q. Huo, **2009**, *81*, 9425.

[45] F. Li, M. Griffith, Z. Li, S. Tanodekaew, H. Sheardown, M. Hakim, D. J. Carlsson, *Biomaterials* **2005**, *26*, 3093.

[46] D. Kuckling, M. E. Harmon, C. W. Frank, *Macromolecules* **2002**, *35*, 6377.

[47] M. M. Islam, V. Cepla, C. He, J. Edin, T. Rakickas, K. Kobuch, Ž. Ružele, W. B. Jackson, M. Rafat, C. P. Lohmann, R. Valiokas, M. Griffith, *Acta Biomater.* **2015**, *12*, 70.

[48] L. Koh, M. Islam, D. Mitra, C. Noel, K. Merrett, S. Odorcic, P. Fagerholm, W. Jackson, B. Liedberg, J. Phopase, M. Griffith, *J. Funct. Biomater.* **2013**, *4*, 162.

Table of contents

A collage-based pro-regenerative pre-medicated corneal implant is developed. By incorporating nanosystem, the advanced functional implant is capable of being infection responsive, promoting regeneration including non-invasive monitoring of in situ corneal environment. These implants further transformed into theranostic devices which are able to respond to biological changes following implantation.

Keyword: Cornea implant, Pro-regeneration, Theranostics, Herpes simplex virus type 1 (HSV-1), Magnetic resonance imaging (MRI)

H. K. Patra*, M. Azharuddin, M. M. Islam, G. Papapavlou, S. Deb, J. Osterrieth, G. H. Zhu, T. Romu, A. K. Dhara, M. J. Jafari, A. Gadheri, J. Hinkula, M. S. Rajan, N. K. H. Slater

Rational nanotoolbox with theranostic potential for medicated pro-regenerative corneal implants

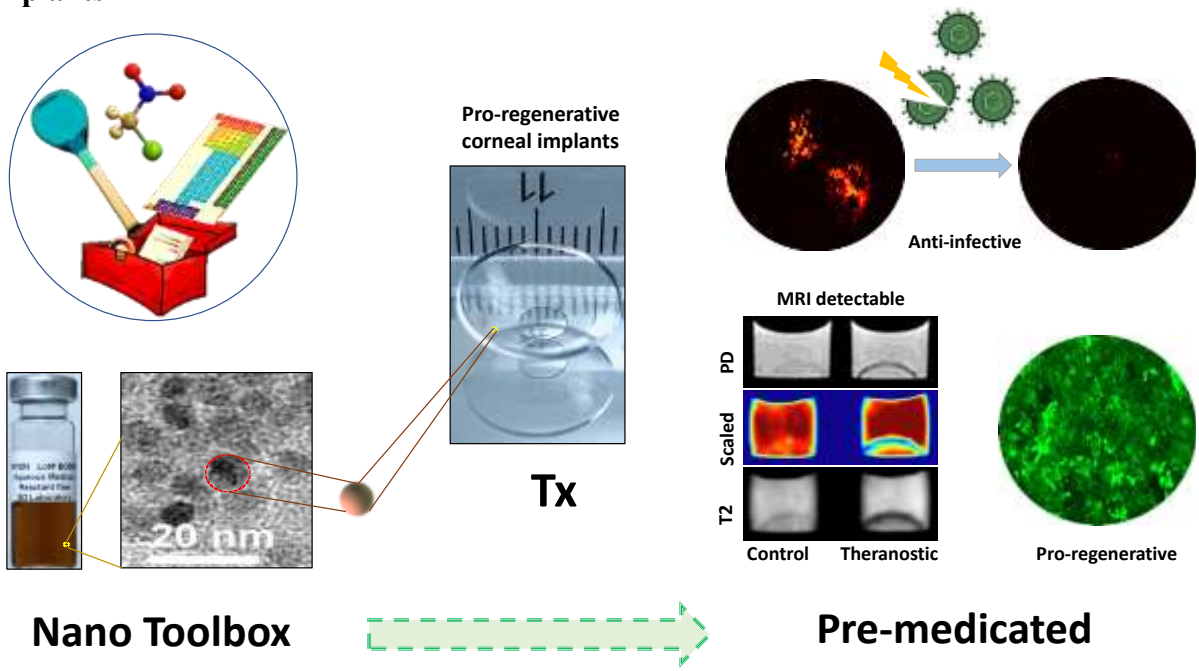

Supporting Information

Rational nanotoolbox with theranostic potential for medicated pro-regenerative corneal implants

Hirak K. Patra, Mohammad Azharuddin, Mohammad M. Islam, Georgia Papapavlou, Suryyani Deb, Johannes Osterrieth, Geyunjian Harry Zhu, Thobias Romu, Ashis K. Dhara, Mohammad J. Jafari, Amineh Gadheri, Jorma Hinkula, Madhavan S Rajan, Nigel K. H. Slater*

Supplementary Information

Section1: Nanoparticle toolbox for ACV conjugation and development of Tx implants

GNPs were synthesized by wet-chemical reduction method using tri-sodium citrate as a reducing and capping agent (S1a). The UV-Vis absorption spectra of the different GNPs (GNP1-GNP5) demonstrated a peak absorbance that varied between 517-551nm (S1b).

a $6Ctr^{3-} + 26AuCl_4^- + 24H_2O \xrightarrow{90°C} 26Au + 6CH_2O + 3HCOOH + 27CO_2 + 104Cl^- + 60H^+$

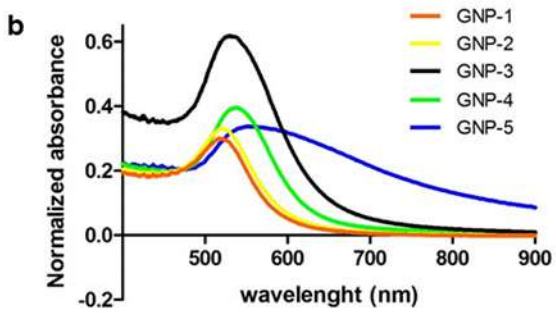

NP name	SPR max (nm)	Citrate concentration (μM)
GNP-1	517	1200
GNP-2	520	600
GNP-3	530	400
GNP-4	539	200
GNP-5	551	100

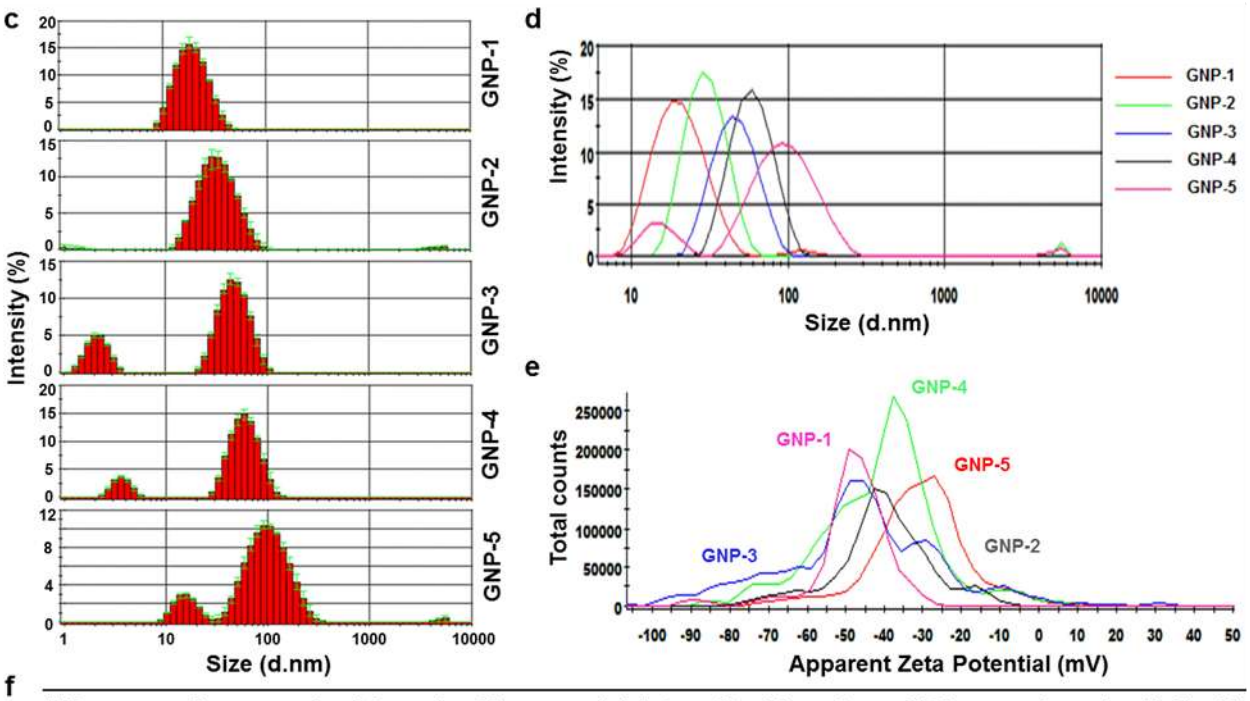

f

NP name	Average size (d. nm)	Mean peak 1 intensity (d. nm)	PDI	zeta potential (mV)
GNP-1	18.17	21.23	0.152	-49.3
GNP-2	32.67	30.74	0.232	-42.8
GNP-3	43.82	47.53	0.967	-45.7
GNP-4	58.77	60.6	0.697	-37.5
GNP-5	105.7	102.7	0.459	-27

Figure S1: Summary of the synthesis of different GNPs: **a** Citrate reduction of aqueous auric chloride solution **b** Surface Plasmon absorption of different GNPs **c** Hydrodynamic diameter and the statistical size distribution of the synthesized GNPs **d** Comparative Dynamic Light Scattering (DLS) profile of the synthesized GNPs **e** Relative zeta potential and **f** summary table of all the GNPs

The shift of the Plasmon Resonance absorption peak to higher wavelength with decreasing citrate concentration indicates an increase in size and changes on Surface Plasmon's. The study of DLS indicated the hydrodynamic size distribution of the different GNPs with their frequency distribution ranging from 18nm for the smaller particles (GNP1) to 110nm for the largest ones (GNP5) (Figure S1c). The comparative distribution indicated the mean intensity of the major

peak as shown in (*Supplementary Figure S1d*). The zeta potential showed a gradual decrease in the surface negative charge, from -52.5mV to -29.6mV, with decreasing citrate concentration (Figure S1e). A higher zeta potential indicates stronger electrostatic repulsion between adjacent particles and a more stable system, which is very important in the later stage of conjugation and integration into the hydrogel. Table f (Figure S1) summarizes the hydrodynamic properties of the synthesized GNPs (GNP1-GNP5) along with the absorption maxima and concentration of citrate used.

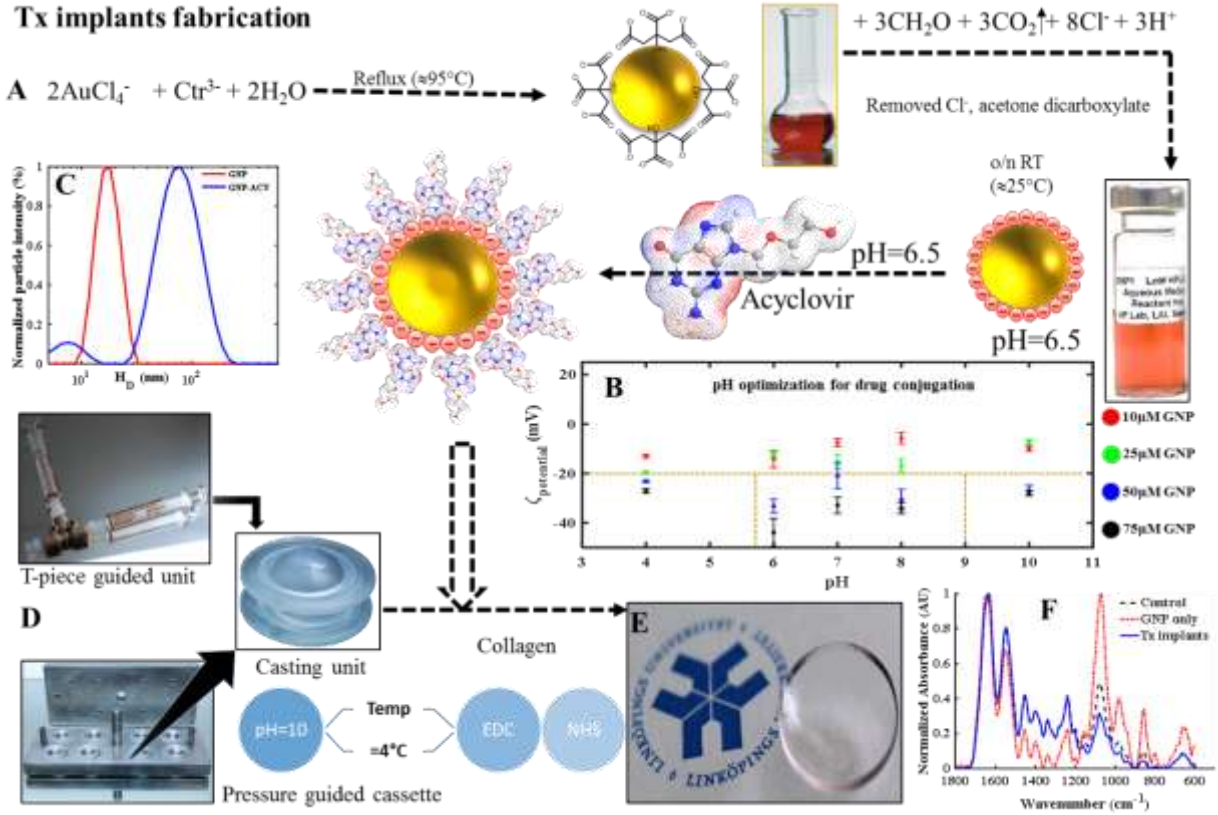

Figure S2. Schematic workflow for **A-C** development of Tx using gold nanosystem with optimized conditions. In the lower panel **D** Tx fabrication strategy using T-piece guided mixing and pressure guided jigs with 500μm molds casting unit described with their respective **E** physical form and **F** molecular signatures. Detailed chemical signature and conjugations are described in *supplementary section 3*.

We have found that the synthesized GNPs are biocompatible to human corneal epithelial cells (HCEC) (*supplementary section 5 and Figure S8)* and therefore theoretically any of them can be used. However, we think that GNP-1 to GNP-3 are suitable for ACV conjugation. The colloidal stability of GNP-4 and GNP-5 could limit the scope due to their higher hydrodynamic diameter and effective size-zeta criticality[1]. We have used GNP-1 as our candidate for the present report. The fabrication set-up and workflow for Tx implant formulation is illustrated in Figure S2.

Section 2: Quantification of morphological changes between control and Tx implants

Methodology

Scanning electron microscopy (SEM) is extensively used to study structural details on the surface of biological samples. The Control and Samples images are compared based on texture analysis. We have cropped several patches of size 200×200 pixels from sample and control images for comparison. Patches created from BSE and SE is shown in Figure S3 and Figure S4, respectively. The comparative study was performed using the patches of samples and control images from BSE and SE, separately.

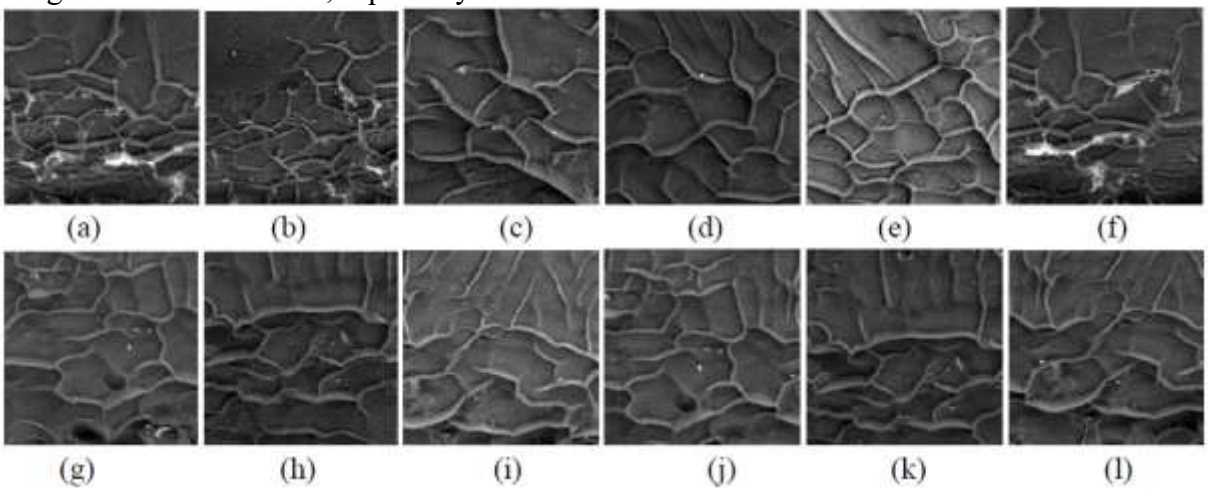

Figure S3. **a-f** patches of control and **g-l** patches of samples in BSE

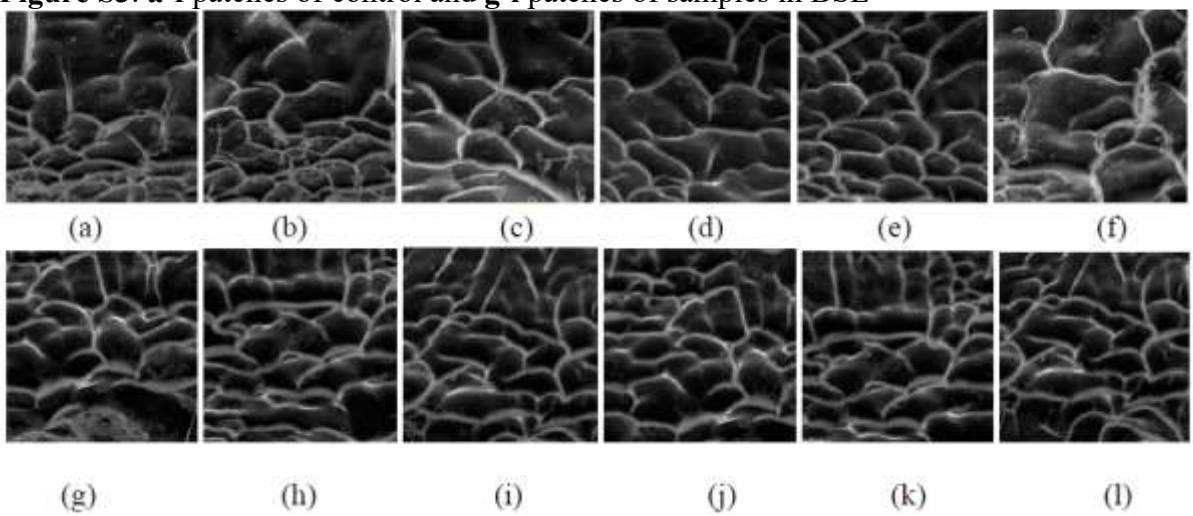

Figure S4. a-f patches of control and **g-l** patches of samples in SE

Morphological change analysis based on Haralick's texture features

Haralick's texture features[2] are the most commonly used measures of texture, which are computed from the gray-level co-occurrence matrix (GLCM). GLCM is formulated by counting the occurrences of different combinations of gray levels of pixels, separated by a specified distance l and a specified angle ψ. The $(i,j)^{th}$ element of a normalized GLCM $p_{(l,\psi)}(i,j)$ with distance l and a specified angle ψ is defined as the probability of occurrence of the pair of gray levels (i, j) at a distance l and at an angle ψ. Mathematically, it can be represented as

$$p_{(l,\psi)}(i,j) = \frac{1}{N_x N_y} | \{(x_1,y_1),(x_2,y_2) \in (N_x \times N_y) | I_q(x_1,y_1) = i,; I_q(x_2,y_2) = j;$$

$$\max(| x_2 - x_1 |,| y_2 - y_1 |= l; \angle[(x_1,y_1),(x_2,y_2)] = \psi\}$$

where, $N_x \times N_y$ is the size of the image under consideration, I(x, y) represents the intensity at a pixel (x, y), and Iq(x, y) is the corresponding quantized intensity value with quantization level Nq. Inverse different moment, a measure of local homogeneity and sum entropy, a measure of non-uniformity in the image are used for comparison of sample and control images. Considering p(I, j) = $(i, j)^{th}$ element of the GLCM matrix, inverse different moment and sum entropy can be computed from the set of sample and control patches and taken average over number of patches. Percentage change of mean inverse different moment and mean sum entropy is used to indicate the quantitative analysis as shown in Table ST1. Percentage change is defined as
Percentage change = Value of a feature in (Control image - sample image) / Value of the feature in the control image. Percentage change of inverse different moment and sum entropy based on 12 set of patches are provided in Table ST2.

Table ST1. Definition of inverse different moment and sum entropy

Feature no.	Feature name	Description
1	Inverse different moment	$\sum_{i=0}^{N_q-1}\sum_{j=0}^{N_q-1}\frac{1}{1+(i-j)^2}p\ (i,j)$
2	Sum entropy	$H^2 = -\sum_{k=0}^{2(N_q-1)} p_{x+y}(k)log_2[p_{x+y}(k)]$

Table ST2. Percentage change of inverse different moment and sum entropy based on 12 set of patches

Image type	Inverse difference moment (%)	Sum entropy (%)
BSE	0.81	1.16
SE	8.48	14.05

Morphological change analysis based on Histogram of oriented gradient (HOG)
HOG features[3] capture edge or gradient structure that is an important characteristic of local shape. It does not affect by local geometric and photometric transformations: translations or rotations make little difference if they are much smaller that the local spatial or orientation bin size. The basic idea is that local object appearance and shape can often be characterized rather well by the distribution of local intensity gradients or edge directions, even without precise knowledge of the corresponding gradient or edge positions. In practice this is implemented by dividing the image window into small spatial regions. Over the pixels of the cell, a local 1-D histogram of gradient directions or edge orientations is computed. The combined histogram is obtained by concatenating all local histogram.
Orientation of gradient are visualized for an example sample and control images in Figure S4. Values of HOG features for sample of Figure S5 (a) and control of Figure S5 (b) are shown in Fig. S6 (a) and Fig. S6 (b). The plot depicts that normalized histogram of gradients features are having similar profile for both example sample and control images. Euclidean distance is computed for the feature sets obtained from control and sample set of cropped BSE and SE images, respectively. Box plot of Euclidean distance is shown in Fig. S6 and results indicate small difference in feature space.

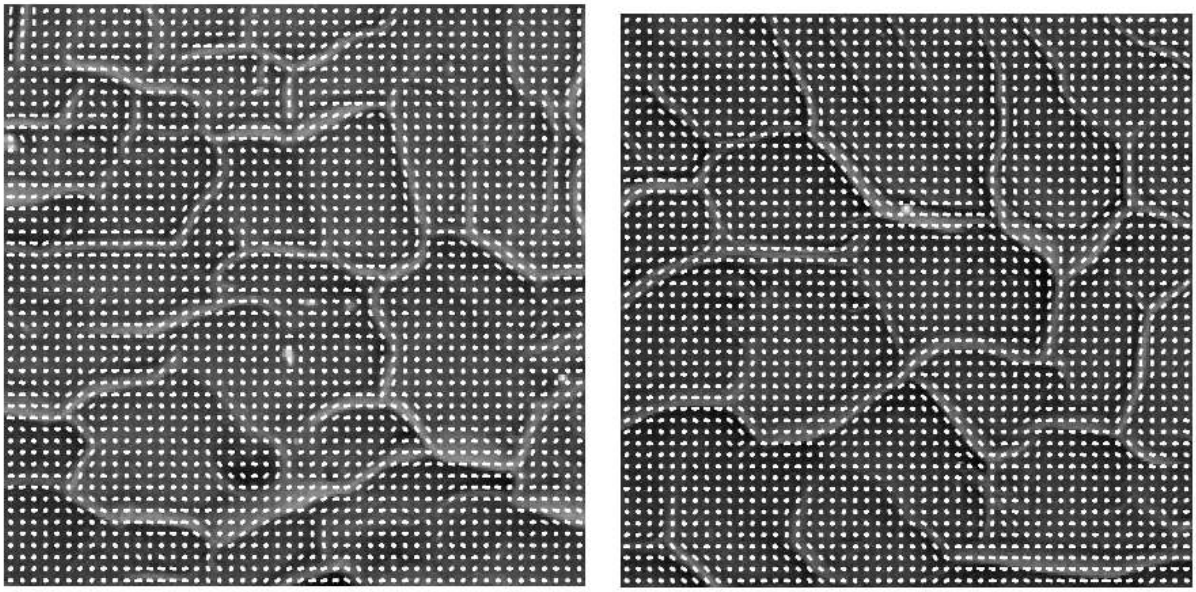

A B

Figure S5. (A) Orientation of gradient in Tx implant with respect to (B) control sample for BSE

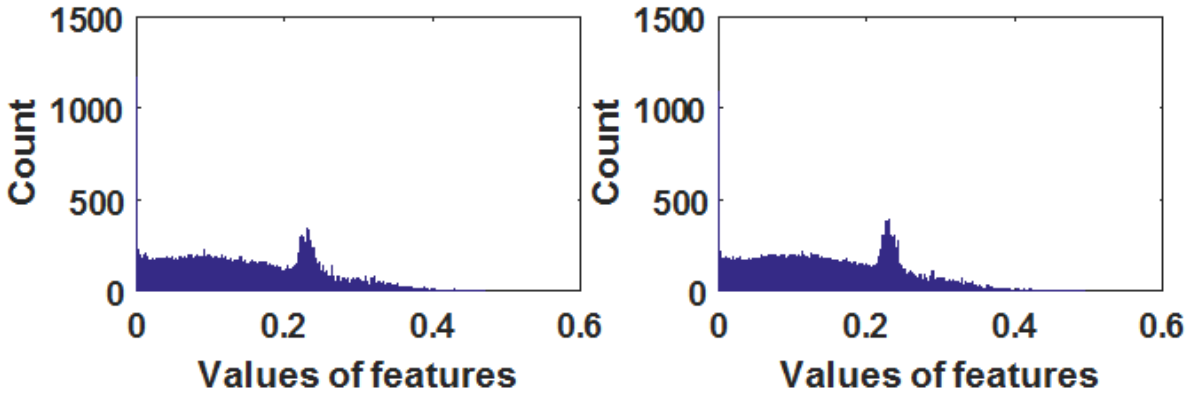

Figure S6. Histogram of values of HOG features for sample of Figure S5 a (left) and control Figure S5b (right)

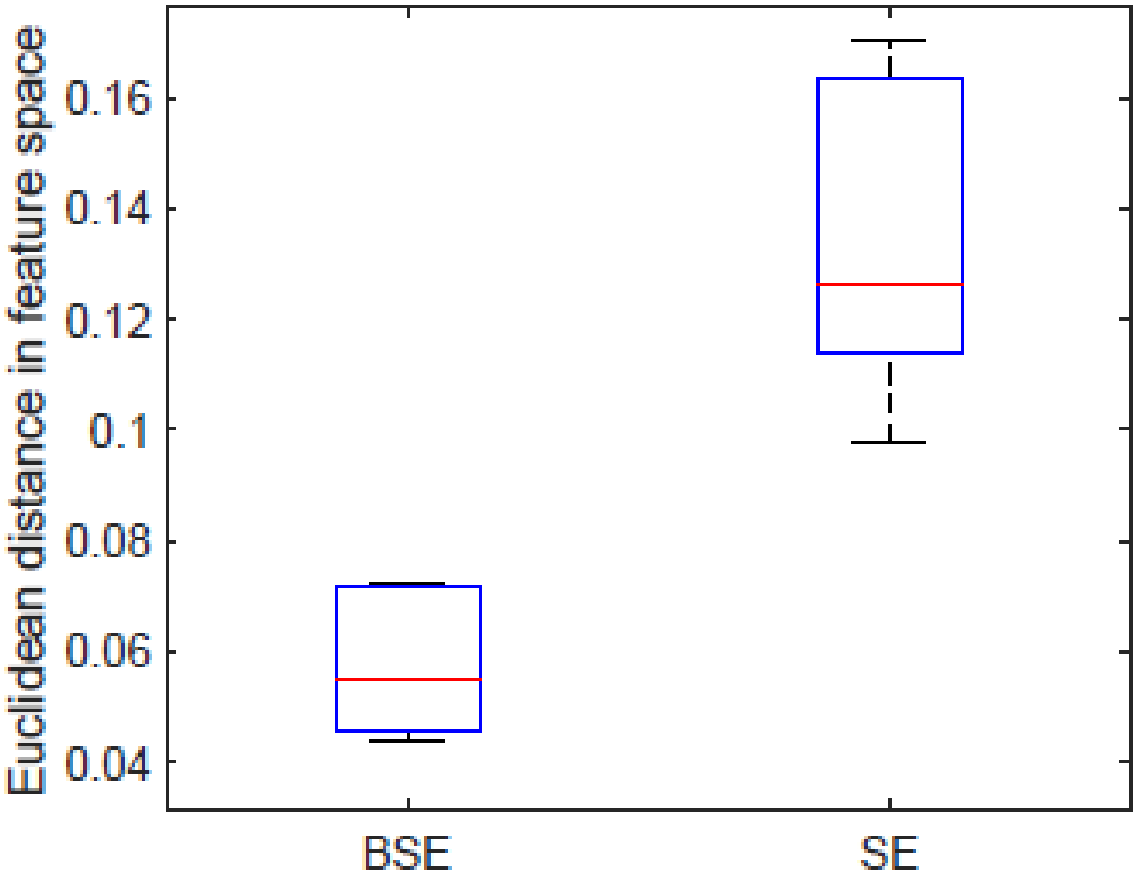

Figure S7. Elaborated Box plot of Euclidean distance in feature space as described in figure 2h. In each box, the central mark is the median, the edges of the box are the 25th and 75th percentiles.

Summary remarks

Following are the remarks: (i) Haralick's texture feature[2] analysis reveal that local homogeneity and non-uniformity in the Tx implants and control image patches are similar and (ii) Small difference of HOG features of sample image set and control image set, indicating similarity in structural features in image content.

Section 3: Fourier Transformed Infrared Spectroscopy

GNP – ACV conjugation study: The primary principle of FT-IR spectroscopy is to detect or probe differences on the molecular level arising from changes between the intra and intermolecular interactions[4]. In this study, we have performed ATR-mode FT-IR for demonstrating the intermolecular changes as a result of conjugation between GNP with ACV. In the spectral range from 1300-1000 cm^{-1}, where the C-O vibrations are located, there is marked difference in the number of peaks[5]. In case of ACV, there are 10 peaks whereas the bio conjugated GNP-ACV has only a single in this specified spectral region. In the spectral region 1700-1450 cm^{-1}, the GNP1-ACV conjugate has only one peak at 1638 cm^{-1} as opposed to the unconjugated ACV which has 6 different peaks. This difference can be ascribed to alterations of C-C, carbonyl, and C-N stretching frequencies[6]. Remarkably, in the region 3600-3200 cm^{-1}, the bio conjugated GNP-ACV depicts additional FT-IR spectral absorption peak which are very distinct as shown in Table ST3.

Table ST3: Summary of peak positions of the FT-IR spectra of ACV and GNP-ACV

Spectral Range (cm^{-1})	ACV	GNP1-ACV
1300-1000	Ten peaks at 1011, 1032, 1047, 1080, 1103, 1180, 1215, 1242, 1281 and 1308	1011
1700-1450	Six peaks at 1483, 1541, 1576, 1611, 1630 and 1703	1638
3600-3200	Four peaks at 3291, 3437, 3468 and 3516	Fifteen peaks at 3208, 3223, 3237, 3246, 3296, 3302, 3318, 3337, 3364, 3379, 3402, 3420, 3466, 3512 and 3584

Tx study: Structural analysis of the control and Tx constructs were done using Attenuated Total Reflectance FT-IR (ATR-FT-IR) on dry solid samples for both nanomaterials and collagen hydrogel constructs. All the experiments were performed using Bruker Vertex 70 spectrometer equipped with a wide range of accessories for ATR. Scans were conducted from the spectra range of 4000-600 cm^{-1} with 72 repetitions averaged for individual spectrum. The standard spectral resolution of better than 0.4 cm^{-1}.

ATR-mode FT-IR spectroscopic studies were performed in order to elucidate the chemical composition and structural integrity of the formed collagen hydrogel bio-constructs, namely, (i) control hydrogel construct without any drug or nanomaterials imbibed in it, (ii) citrate stabilized GNP1 entrapped hydrogel and (iii) bioconjugated GNP1-ACV entrapped collagen hydrogel. The distinct characteristics amide bands displayed by collagen via FT-IR spectral analysis can reveal an intriguing insight into its triple helical structural integrity[7] as shown in Table ST4[8,9]. The table clearly demonstrate that the cross-linked collagen hydrogel bio-constructs synthesized does not show any detectable band shift in comparison to the band positions of native collagen reported earlier[10]. This information leads to one of the most important observations that the in spite of the cross-linking agents and drug/nanomaterials entrapped inside the collagen hydrogel, the triple helical organisation of the collagen chains remains intact in the above mentioned bio-constructs. In addition to the unchanged peak/band positions of distinct amide bands, we have also calculated the ratio of absorbance between $amide_{III}$ to 1450 cm^{-1} (Abs_{III}/Abs_{1450}) band. This ratio particularly depicts the degree of triple

helix preservation following the formation of cross-linked collagen hydrogel constructs[9][10]. A ratio of (Abs_{III}/Abs_{1450}) (Table ST5, Figure S2) closer to unity provide evidence of the preserved triple helical integrity of the formed collagen networks, which is an integral aspect of our study because if the structural integrity of the collagen hydrogel bio-constructs is compromised following the entrapment of conjugated/unconjugated GNP1, then it will lead to an instant graft rejection.

Table ST4: Peak position and band vibrations of different collagen hydrogel bio-constructs

	Hydrogel-Control	**Hydrogel-GNP1**	**Hydrogel-GNP1-ACV**	**Chemical composition**
Peak position (cm^{-1})	3294 and 3100	3289 and 3103	3296 and 3080	Amide A and B bands-associated with the stretching vibrations of N-H groups[4]
Peak position (cm^{-1})	1634 and 1547	1647 and 1549	1632 and 1547	Amide I and II bands- these primarily results from the stretching vibrations of peptide C=O groups and as well as from N-H bending and C-N stretching vibrations[4]
Peak position (cm^{-1})	1238	1238	1238	Amide III band- this is assigned to the C-N stretching vibrations as well as N-H bending vibrations from the amide linkages.[4]
Peak position (cm^{-1})	1450	1452	1452	

Table ST5: Ratio of absorbance at 1250 cm^{-1} and 1450 cm^{-1}

	Hydrogel-Control	**Hydrogel-GNP**	**Hydrogel-GNP-ACV**
Ratio (Abs_{III}/Abs_{1450})	1.026	1.017	0.966

Section 4: Properties of Tx implants

The functional integrities and implicit requisites of the formulated Tx implants were tested and compared with the control (Bs, without nanosystems). Physical and biocompatibility properties of the implants are described in Figure S8.

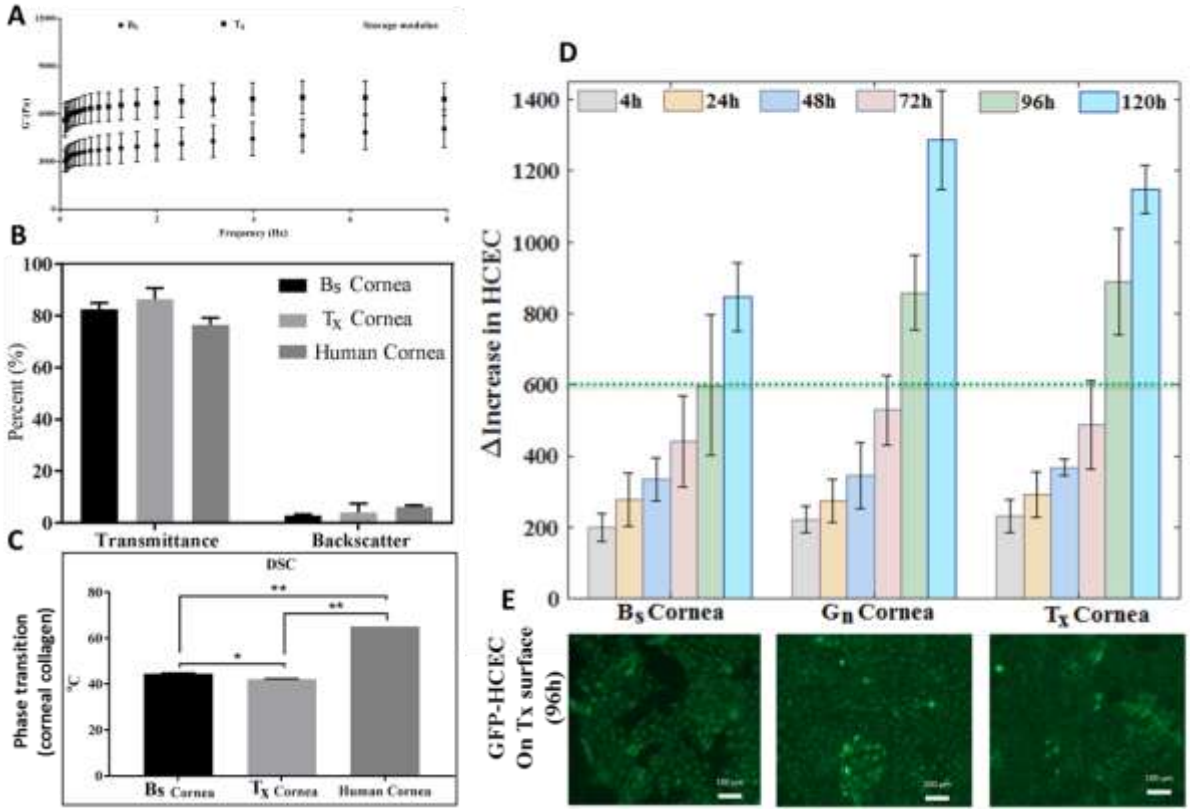

Figure S8: Functional characterization of Tx implants compared to unmodified controls. (**A**) Storage modulus of the samples (**B**) Optical transmittance and back scattering of control and Tx implants(**C**) Differential scanning calorimetry (DSC) of implants (**D**) Proliferation rates of human corneal epithelial cells (HCECs) on Tx, unmodified control implants (Bs) and implants with GNPs only without drugs (Gn cornea) (**E**) Fluorescence microscopic images of GFP-HCECs layer on the different implants at 96 hours post-seeding.

Viscoelastic properties of the hydrogels were tested with rheometer. The storage modulus (G′) is the ability to store deformation energy in an elastic manner during shear process of material.

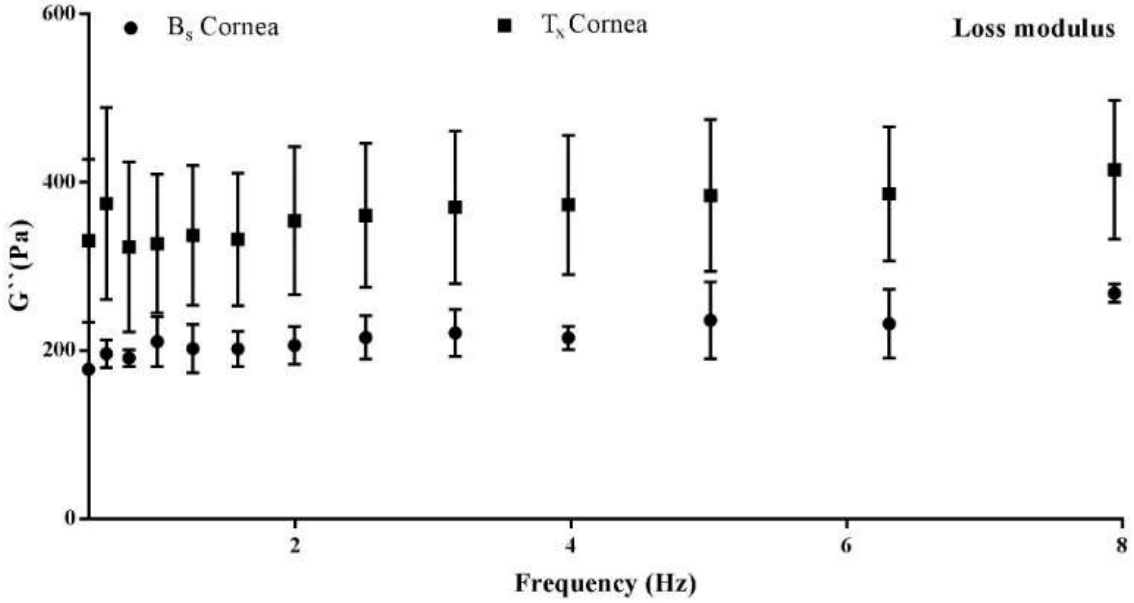

Figure S9. Comparative Loss modulus

This is directly proportionate to the degree of cross-linking, meaning that the higher the degree of cross-linking correlates with the greater storage modulus. In other way, higher G' denotes more solid-like property, higher strength and mechanical rigidity. Comparing control (Bx) to Tx showed that, Tx had high storage modulus proving that Tx was mechanically strong than Bx, although denaturation temperature of the Bx was high then Tx.

Section 5: Growth promotion activity of GNPs on human corneal epithelial cells

MTS assay was performed to estimate the growth promoting rate of HCECs in the presence of different concentrations of the GNPs (10, 25, 50 and 100 μM). Regardless the incubation period (12, 24 or 48 h), cell survival followed a similar pattern. No significant cytotoxicity observed with any of the GNPs examined (Figure S8 a-c).

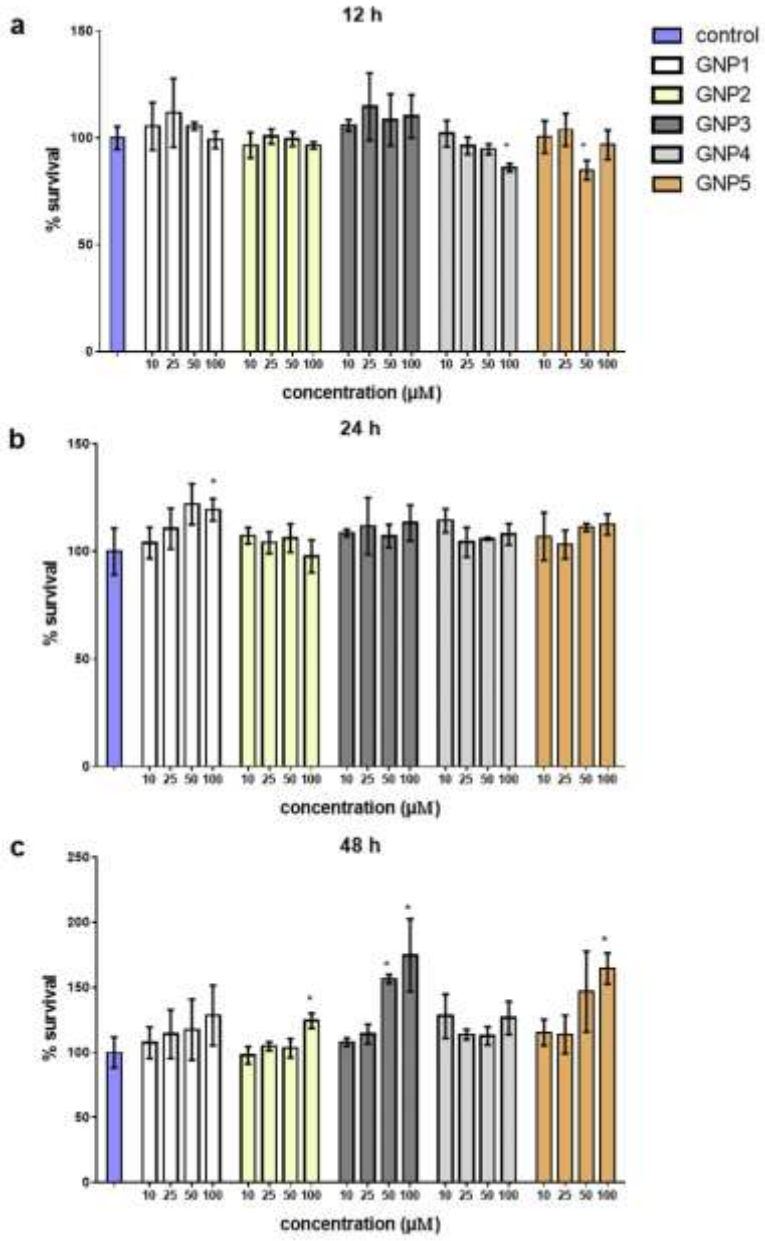

Figure S10. GNP Proliferation. Percentage survival of HCECs after incubation with increasing concentrations of the different GNPs for (a) 12 h (b) 24 h and (c) 48 h. Cell viability was assessed by the MTS assay and the absorbance was recorded at 490 nm. Data are presented as mean ± standard deviation (n = 3). Unpaired t-test was performed and significance was defined as $p < 0.05$. The asterisk * indicates significant difference compared with the control.
Remarkably, GNPs 2, 3 and 5 demonstrated a higher percentage of cell survival for the highest concentration.

Section 6: Biocompatibility of FeNPs on HCECs

Cell viability (MTS) assay was performed on HCECs in the presence of increasing concentrations of the FeNPs (10, 25, 50 and 100μM) for 12, 24 and 48 hrs. In spite of the increasing dose of FeNPs, cell survival percentage for HCECs remains the same, with more than 80% survivality even after 48hrs of incubation. No observable cytotoxity was observed for the nanoparticles (Figure S11). This result indicates that FeNPs can be a reasonable candidate for theranostic applications.

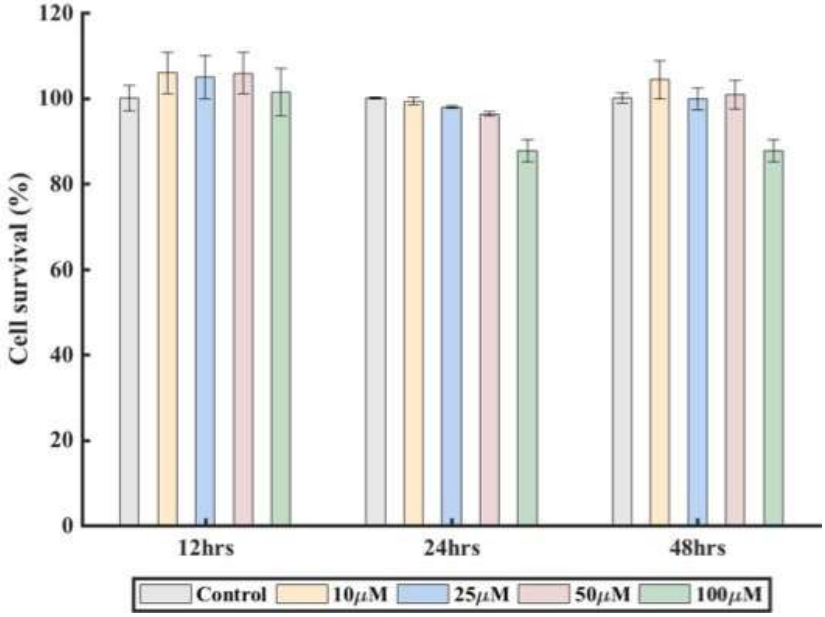

Figure S11. FeNPs cytotoxicity assay: Percentage survival of HCECs after incubation with increasing concentration of FeNPs from 10-100μM for 12, 24 and 48 h. MTS assay were performed for cell viability assay and absorbance was recorded at 490nm. We have optimized the safe concentration of FeNPs for the design of theranostic biosynthetic corneas. Data are presented as mean ± standard deviation (n=3). Unpaired t-test was performed and significance was defined as $p<0.05$.

Section 7: Electron microscopic study

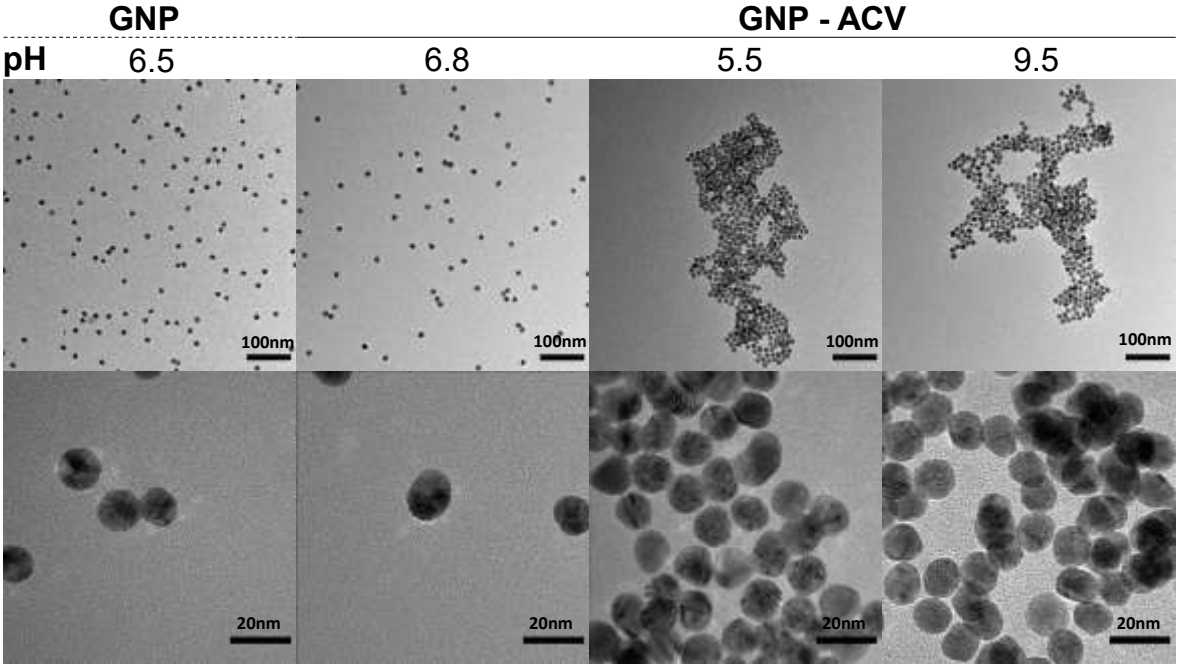

Figure S12. The detailed electron microscopic characterisation of gold nanoparticles (GNP), while loaded with drug (GNP-ACV) and GNP-ACV at low (5.5) and high (9.5) pH. The upper panel showing that overall distribution and features of the nanoparticles and the lower one showing the overall distribution and features of the nanoparticles and the lower one is showing the respective feature with higher magnification.

Section 7: Potential and prospective applications of Tx implants in Corneal pathogenesis

By 2019, it is estimated that 84% of all visual impairment will be among those aged 50 years or more.

Diseases	Broad reason	Specific reason	Treatment option	Potential Tx remedy	Tried in this paper
Infections					
	Bacterial	*Pseudomonas aeruginosa, Viridans streptococci, Staphylococcus aureus*	Anti-bacterial/ Artificial cornea transplantation	Yes	
	Fungal	*Candida albicans, Fusarium solani*	Anti-fungal/ Artificial cornea transplantation	Yes	
	Viral	Herpes simplex virus (HSV)	Anti-viral/ Artificial cornea transplantation	Yes	Yes
Trauma					
	Exposure to toxic chemicals	Alkali burn, acid burn	Artificial cornea transplantation	Yes	
Dystrophies and degenerative corneal disorders					
	Fuchs' dystrophy	Dysfunctional endothelium	Artificial cornea transplantation	Yes	
	map-dot-fingerprint dystrophy	Developmental defect of epithelium's basement membrane	Artificial cornea transplantation	Yes	
Ectasia (thinning)					
	Keratoconus	Normally round cornea becomes thin and develops a cone-like bulge	Artificial cornea transplantation	Yes	
Stevens-Johnson syndrome					
	Toxic epidermal necrolysis	Immune-complex–mediated hypersensitivity complex	Early recognition and withdrawal of all potential causative drugs	Yes/No	MRI monitoring could be useful
Human donor cornea transplantation associated diseases					
	Disease transmission	Transmission of HSV from donor to host	Artificial cornea transplantation	Yes	
	Immunosuppression	Compromise immune system, Activate latent HSV	Artificial cornea transplantation	Yes	
	Reactivation of pathogen	Reactivation of HSV during transplantation	Transplant containing anti-microbial agent	Yes	Yes
Treatment approach related complications					
	Requirement of huge dose of drug	Less amount of drug reach at the point of interest	Nano-carrier based drug delivery	Yes	Yes
	High dosage regimen	To keep effective concentration	Sustained release drug delivery	Yes	Yes
	Systemic side effect	Gastrointestinal upset	Devilry of drug from carrier through artificial cornea	Yes	Yes
	Resistance/latency formation by pathogen	Inefficient amount of drug at the site of action	Local drug delivery	Yes	Yes

References

[1] H. K. Patra, A. K. Dasgupta, *Nanomedicine Nanotechnology, Biol. Med.* **2012**, *8*, 842.
[2] R. M. Haralick, K. Shanmugam, I. Dinstein, *IEEE Trans. Syst. Man. Cybern.* **1973**, *SMC-3*, 610.
[3] N. Dalal, W. Triggs, *2005 IEEE Comput. Soc. Conf. Comput. Vis. Pattern Recognit. CVPR05* **2004**, *1*, 886.
[4] G. E. McGuire, M. A. Ray, S. J. Simko, F. K. Perkins, S. L. Brandow, E. A. Dobisz, R. J. Nemanich, A. R. Chourasia, D. R. Chopra, *Anal. Chem.* **1993**, *65*, 311.
[5] T. L. Threlfall, *Analyst* **1995**, *120*, 2435.
[6] K. M. Lutker, R. Quiñones, J. Xu, A. Ramamoorthy, A. J. Matzger, *J. Pharm. Sci.* **2011**, *100*, 949.
[7] E. Leikina, M. V. Mertts, N. Kuznetsova, S. Leikin, *Proc. Natl. Acad. Sci.* **2002**, *99*, 1314.
[8] R. S. Walton, D. D. Brand, J. T. Czernuszka, *J. Mater. Sci. Mater. Med.* **2010**, *21*, 451.
[9] X. Zhang, L. Xu, X. Huang, S. Wei, M. Zhai, *J. Biomed. Mater. Res. - Part A* **2012**, *100 A*, 2960.
[10] G. Tronci, A. Doyle, S. J. Russell, D. J. Wood, *J. Mater. Chem. B* **2013**, *1*, 5478.